

Numerical Forecasts of the 15–16 June 2002 Southern Plains Mesoscale Convective System: Impact of Mesoscale Data and Cloud Analysis

DANIEL T. DAWSON II AND MING XUE

School of Meteorology, and Center for Analysis and Prediction of Storms, University of Oklahoma, Norman, Oklahoma

(Manuscript received 31 January 2005, in final form 11 August 2005)

ABSTRACT

High-resolution explicit forecasts using the Advanced Regional Prediction System (ARPS) of the 15–16 June 2002 mesoscale convective system (MCS) that occurred over the U.S. central and southern plains during the International H₂O Project (IHOP_2002) field experiment period are performed. The forecasts are designed to investigate the impact of mesoscale and convective-scale data on the initialization and prediction of an organized convective system. Specifically, the forecasts test the impact of special mesoscale surface and upper-air data collected by, but not necessarily specific to, IHOP_2002 and of level-II data from multiple Weather Surveillance Radar-1988 Doppler radars. The effectiveness of using 30-min assimilation cycles with the use of a complex cloud-analysis procedure and high-temporal-resolution surface data is also examined. The analyses and forecasts employ doubly nested grids, with resolutions of 9 and 3 km. Emphasis is placed on the solutions of the 3-km grid. In all forecasts, a strong, well-defined bow-shaped MCS is produced with structure and behavior similar to those of the observed system. Verification of these forecasts through both regular and phase-shifted equitable threat scores of the instantaneous composite reflectivity fields indicate that the use of the complex cloud analysis has the greatest positive impact on the prediction of the MCS, primarily by removing the otherwise needed “spinup” time of convection in the model. The impact of additional data networks is smaller and is reflected mainly in reducing the spinup time of the MCS too. The use of intermittent assimilation cycles appears to be quite beneficial when the assimilation window covers a time period when the MCS is present. Difficulties with verifying weather systems with high spatial and temporal intermittency are also discussed, and the use of both regular and spatially shifted equitable threat scores is found to be very beneficial in assessing the quality of the forecasts.

1. Introduction

In recent years, an increasing amount of interest in the numerical weather prediction (NWP) community has focused on the problem of storm-scale (or convective scale) prediction. Any attempt at resolving and accurately predicting atmospheric phenomena on these scales must address several factors. They include, but are not limited to, sufficient horizontal resolutions to resolve storm-scale features; appropriate model physical parameterizations for turbulence, microphysics, and surface processes; and robust initialization strategies for providing accurate model initial conditions. This study focuses on the last issue.

One of the most important components of any NWP

system is the forecast initial conditions and the procedure by which such conditions are obtained. The initial condition is generally obtained through the ingesting and processing of observations that are then combined in some statistically optimal manner, for example, through the optimal interpolation (OI) method, with a “first guess” or “background” field that is usually taken from a model forecast (e.g., Lorenc 1981; Parrish and Derber 1992). Other methods for producing analyzed fields include three-dimensional variational data assimilation (3DVAR; e.g., Courtier et al. 1998; Gao et al. 2004), four-dimensional variational data assimilation (4DVAR; e.g., Rabier et al. 2000; Sun and Crook 2001), and the newer ensemble Kalman filter method [EnKF; see, e.g., Snyder and Zhang (2003), Dowell et al. (2004), and Tong and Xue (2005) for examples of assimilating simulated radar data for convective storms]. As in OI, all these methods produce an analyzed field through the “optimal” blending of some first-guess field with observational data. In fact, it can be shown that

Corresponding author address: Dr. Ming Xue, School of Meteorology, University of Oklahoma, 100 East Boyd, Norman, OK 73019.

E-mail: mxue@ou.edu

3DVAR, though formulated differently, is mathematically equivalent to OI under commonly used assumptions. In the cases of 4DVAR and EnKF, the assimilation of data is done over a period of time, in which observations are brought in during a model forecast period. The period during which observational data is ingested into the system is often known as the assimilation window. With one-time assimilation methods such as OI and 3DVAR, the assimilation window can consist of a sequence of (intermittent) assimilation cycles during which the single-time analysis procedure is repeated a number of times, separated by forecast cycles, in order to effectively assimilate data distributed over the assimilation window. At the end of the assimilation cycles or assimilation window, a final analysis is produced that provides the initial condition for a subsequent model forecast. When the initial condition is based on an analysis at a single time, and especially when the analysis background is from the forecast of a different model, the subsequent forecast is often referred to as “cold starting” from such initial conditions.

No matter how the initial conditions are derived, for mesoscale and storm-scale NWP, they should contain sufficient information on the scale of the phenomena being predicted. This is particularly difficult for storm-scale NWP because traditional surface and upper-air observational networks, in general, do not have sufficient spatial resolution to adequately resolve storm-scale features. However, many high-resolution “non-standard” surface data sources do exist, in the form of various special surface networks. When assimilated into a mesoscale/storm-scale NWP model, these data could potentially provide an improvement in the forecast of such events, provided that the model is capable of faithfully reproducing storm-scale convective features. In addition to in situ surface and upper-air observations, observations from the U.S. Weather Surveillance Radar-1988 Doppler (WSR-88D) or Next-Generation Weather Radar (NEXRAD) Doppler radar network can provide very valuable, high-resolution observations of the precipitating regions of the atmosphere that are very important for initializing convective systems.

In this study, we examine the impact of several different data sources and data assimilation strategies on the explicit high-resolution prediction of a severe mesoscale convective system (MCS) that evolved into a bow echo during 15–16 June 2002 over the U.S. central and southern plains. Though the observed system produced large amounts of severe weather (mostly damaging surface winds), no attempt is made in this study to verify or quantify the model’s ability to represent the severe aspects of this system. Rather, the focus is on the

overall evolution of the structure and propagation of the system. This event occurred during the International H₂O Project (IHOP_2002; Weckwerth et al. 2004) field program, during which large amounts of meteorological data were collected or compiled from various observational platforms. We report on the results of forecasts in which many of these special data, particularly those from surface data networks, though not necessarily data specific to IHOP itself, were assimilated into the initial conditions. We compare and contrast these forecasts with those that included only standard data sources, which, for the purposes of this study, include the standard National Weather Service (NWS) Surface Aviation Observation (SAO) network, the rawinsonde observation (raob) upper-air sounding network, and the National Oceanic and Atmospheric Administration (NOAA) Wind Profiler Demonstration Network (WPDN). We also discuss the use of a complex cloud analysis incorporating high-resolution WSR-88D data, and the results of forecasts that include intermittent assimilation cycles. Quantitative scores were calculated for the forecast radar reflectivity fields.

In section 2, the NWP framework, including the analysis component used in this study, is discussed. Section 3 provides an overview of the weather conditions associated with the MCS. Section 4 discusses the methodology for the various experiments conducted in this study and the verification procedures used. Results are discussed in sections 5 and 6, and a summary is given in section 7.

2. The ARPS and ADAS systems

The NWP model used in this study is the University of Oklahoma Advanced Regional Prediction System (ARPS; Xue et al. 2000, 2001, 2003), a general-purpose compressible nonhydrostatic model. The ARPS is capable of simulating and predicting a wide range of atmospheric phenomena on multiple scales, including the storm scale, making it ideally suited for this study.

The ARPS Data Analysis System (ADAS; Brewster 1996; Case et al. 2002; Lazarus et al. 2002) is used for the data analyses and to provide the initial conditions for the various forecasts in this study. The ADAS analysis is based on the Bratseth (1986) successive correction method, which can converge to the OI solution. The basic analysis scheme of ADAS assimilates observational data that are the same as, or can be easily converted to, the model prognostic variables, such as temperature, pressure, humidity, and the horizontal components of air motion. Such data are readily available from standard and nonstandard surface and upper-

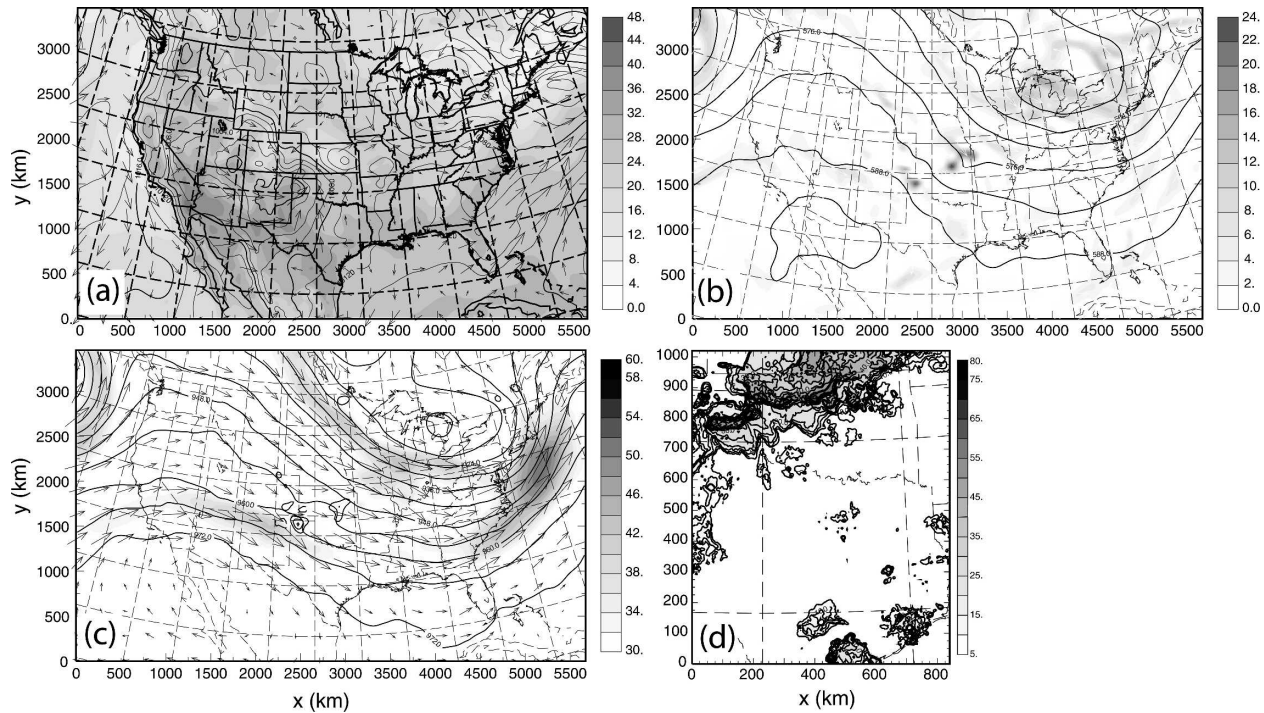


FIG. 1. Weather conditions at 0000 UTC 16 Jun 2002: (a) sea level pressure (contours, 4-hPa increment), surface temperature (shading, 4-K increment), and surface wind vectors; (b) 500-hPa height (contours, 60-m increment) and vorticity (shading, $2 \times 10^{-5} \text{ s}^{-1}$ increment); (c) 300-hPa height (contours, 60-m increment), wind speed (2 m s^{-1} increment), divergence (shading, $0.1 \times 10^{-4} \text{ s}^{-1}$ increment), and wind vectors; and (d) observed composite reflectivity (5-dBZ increment) field of the MCS in northern Oklahoma.

air observational networks. The analysis scheme is three-dimensional and is therefore capable only of producing analyzed fields at a single time. However, when combined with the ARPS prediction model, a four-dimensional intermittent data assimilation system can be established through frequent assimilation cycles. In this study, the ADAS is used in both single analysis configuration and intermittent assimilation cycle mode.

In addition, the ADAS also contains a complex cloud-analysis component (Zhang and Carr 1998; Zhang et al. 1998; Zhang 1999; Brewster 2002; Hu et al. 2006a) that is capable of ingesting Doppler radar, satellite, and surface cloud observations, producing analysis of cloud, rain, and ice water contents, and adjusting humidity and temperature fields. The use of a cloud analysis can significantly mitigate the common “spinup” problem of precipitation forecasts. In the initial conditions of typical large or mesoscale NWP systems, observation-based cloud fields and their attendant thermal fields are generally not present, and the NWP model has to produce or spin up these fields through the course of integration, resulting in poor quantitative precipitation forecasts during the first few hours of the forecast. Such a problem can have a significant impact on the prediction of precipitating sys-

tems, especially during the early parts of the forecast (Zhang 1999). Additional discussions on the spinup issue can be found in Souto et al. (2003), which demonstrated the positive impact of a simple procedure that creates cloud fields in the initial condition but without the use of additional data on the precipitation prediction in a region in Spain. In this work, the impact of radar data on the forecast position and structure of an MCS is examined through the ADAS cloud-analysis procedure. The impact of other more conventional data, from routine and special networks, is also examined.

3. Overview of the 15–16 June 2002 severe MCS

The synoptic-scale environment in the central and southern plains region at 0000 UTC 16 June 2002 was one of northwesterly flow around a mid-to-upper-level low pressure system centered over the Great Lakes region (see Fig. 1). A surface low was present over the northern Texas panhandle (Fig. 1a), and a large, developing severe MCS (Fig. 1d), the focus of this study, was located from the northern Texas panhandle eastward across northern Oklahoma and southern Kansas, just ahead of a midlevel shortwave trough (Fig. 1b). Although this trough appeared to be enhanced by upscale

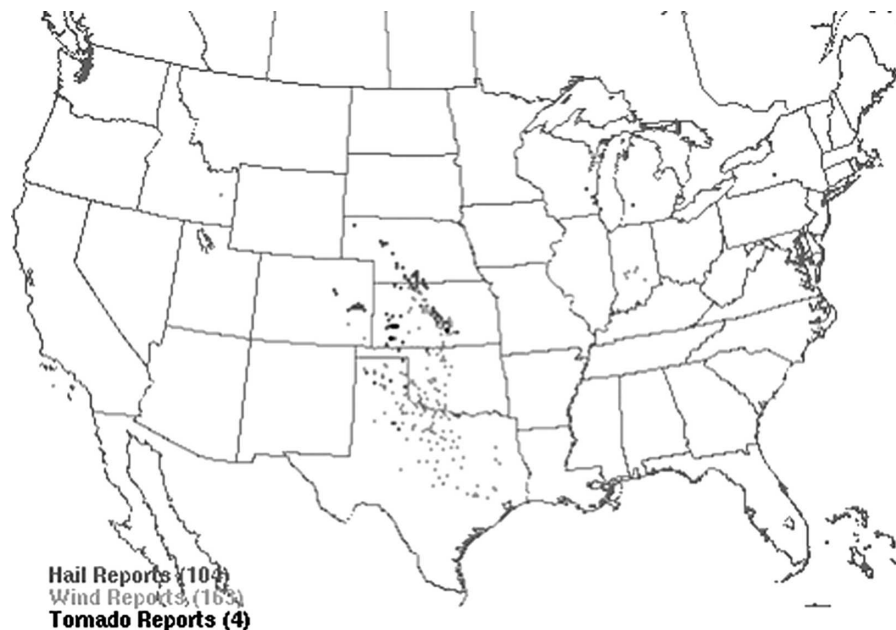


FIG. 2. Storm Prediction Center (SPC) severe weather reports for 15 Jun 2002.

influences of the convection, it was also present before the development of the MCS in the analysis fields 12 h earlier (not shown). A jet streak was present in the southern streamflow extending across northern New Mexico, and upper-level divergence (Fig. 1c) in the left exit region of this feature was helping to force the development of the surface low over the panhandle of Texas. The MCS had already produced severe weather, including a few tornadoes, in southern Kansas by this time, and went on to produce a swath of wind damage reports through central Oklahoma southward through central Texas as it propagated south-southeastward (see Fig. 2).

During the 12-h forecast period that followed, the northwesterly flow regime continued, with the midlevel shortwave moving in tandem with the MCS, and the upper-level jet streak propagating farther southeastward into western Texas (not shown). The surface low continued to move south-southeastward, reaching extreme southwest Texas (not shown) by 1200 UTC 16 June 2002. A low-level jet feature to the east of the surface low continued to feed low-level unstable air into the MCS as it propagated to the south.

4. Experiment design and methodology

a. Forecast configuration

A set of two one-way nested grids was used for the ARPS forecasts in this study (Fig. 3). The horizontal resolutions were 9 and 3 km for the coarse and fine

grids, respectively. The vertical grid on each domain consisted of 50 layers over a 20-km depth in a stretched configuration with a minimum thickness of about 20 m near the surface increasing to nearly 800 m near the model top. The model is used in its full physics mode, including a soil-vegetation model, planetary boundary layer parameterization, ice microphysics, turbulent kinetic energy-based subgrid-scale turbulence, and full longwave and shortwave radiation [see Xue et al. (2001,

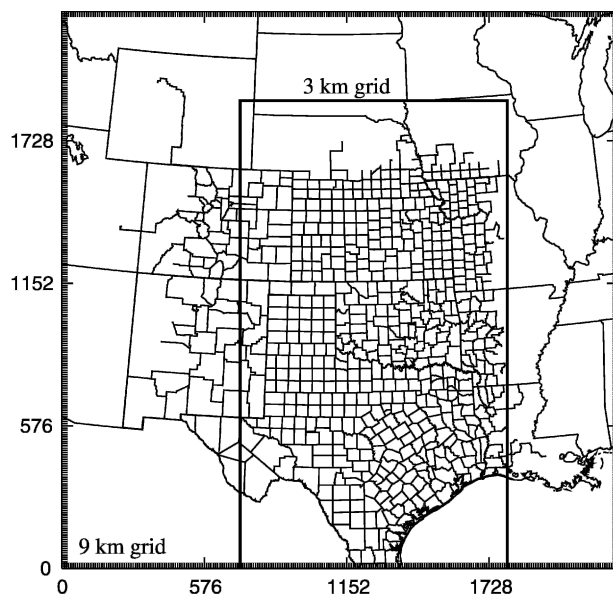


FIG. 3. Computational domains for the 9- and 3-km grids.

TABLE 1. Description and abbreviations of surface and upper-air data networks.

Type of datasets	Dataset description	Abbreviation
Surface datasets	Surface Aviation Observations	SAO
	Oklahoma Mesonet	OKMESO
	Texas Tech West Texas Mesonet	WTXMN
	High Plains Climate Network	HPCN
	Missouri Commercial Agricultural Weather Station Network	MOCAWS
	Texas North Plains Potential Evapotranspiration (PET) Network	TPET
	National Center for Atmospheric Research (NCAR) Atmospheric Technology Division (ATD) Integrated Surface Flux Facility	ISFF
	Colorado Agricultural Meteorological Network	COAG
	U.S. Department of Agriculture (USDA) Agricultural Research Service (ARS) Micronet	ARS
	Department of Energy (DOE) Atmospheric Radiation Measurement (ARM) Southern Great Plains (SGP) Surface Meteorological Observation System (SMOS)	ARMS
	DOE Atmospheric Boundary Layer Experiments (ABLE) Automatic Weather Station (AWS)	ABLE
	National Center for Atmospheric Research Atmospheric Technology Division (NCAR/ATD) supplemental surface meteorological data	NCAR
	NCAR/ATD Homestead Integrated Sounding System observation station	ISS
	Automatic Surface Observing System (5-min data)	ASOS
	Offshore buoy observations	BUOY
	Southwest Kansas Mesonet	SWKS
	Kansas Groundwater Management District No. 5	GWMD
Upper-air datasets	NWS rawinsonde observations	raob
	NWS Meteorological Data Collection and Reporting System Aircraft Observations	MDCRS
	NOAA Wind Profiler Demonstration Network	WPDN

2003) for details on the physics]. The Kain–Fritsch convective parameterization scheme (Kain et al. 2003) was used on the 9-km domain but not on the 3-km domain. Two sets of experiments were performed, one with forecasts starting from 1800 UTC 15 June 2002, when much of the convection associated with the MCS was just beginning to develop and organize, and the other with forecasts starting from 0000 UTC 16 June 2002, at a time when the MCS exhibited a significant level of organization as a well-developed east–west-oriented squall line that was beginning to show bow echo characteristics. The 1800 UTC forecasts were run for 18 h, while the 0000 UTC forecasts were run for 12 h. It was found that the predicted MCS began to depart significantly from that observed after 12 h in the 1800 UTC forecasts, so only the first 12 h of forecast will be discussed. Throughout this paper, we will use the following experiment naming convention, described by the template [9km, 3km][00UTC, 18Z][Eta, St, Ext][C, A, CA]. The brackets denote portions of the experiment name, and the contents of the brackets denote the possible values those portions may have. The first bracket is the horizontal resolution of the experiment domain, the second is the forecast start time, the third is an abbreviation describing the type and amount of data used in the initial conditions, which will be explained later, and the last brackets denote whether a cloud analysis (C), assimilation cycle (A), or both (CA) were

used. For example, experiment 3km18ZExtCA denotes the experiment at 3-km horizontal resolution, with a forecast start time of 1800 UTC, containing “extra” surface data networks in the initial conditions, and using the cloud-analysis procedure in the assimilation cycle mode prior to the 1800 UTC start time.

During the 18-h time period from 1800 UTC 15 June to 1200 UTC 16 June 2002, the MCS quickly developed through the merging of short lines and individual convective cells in western Kansas into a well-organized squall line by 2300 UTC that then propagated from southwestern Kansas/northern Oklahoma to the Texas gulf coast, and thus the computational grids were chosen to cover these areas. The results on the 3-km domain are the primary focus of this study while the primary purpose of the 9-km domain is to provide the boundary conditions for the nested 3-km domain. Table 1 provides a list of all the data sources used for data assimilation in this study, along with their abbreviations. Figure 4 shows the experiment configuration for the main 0000 UTC simulations. The configuration for the 1800 UTC simulations is identical, except that the start time for the assimilation cycles and forecast cycles are shifted back by 6 h. Table 2 gives further details of the assimilation–forecast experiments with the 0000 UTC forecast start time. Finally, Fig. 5 shows the locations of surface and upper-air stations as used in the 3-km forecasts.

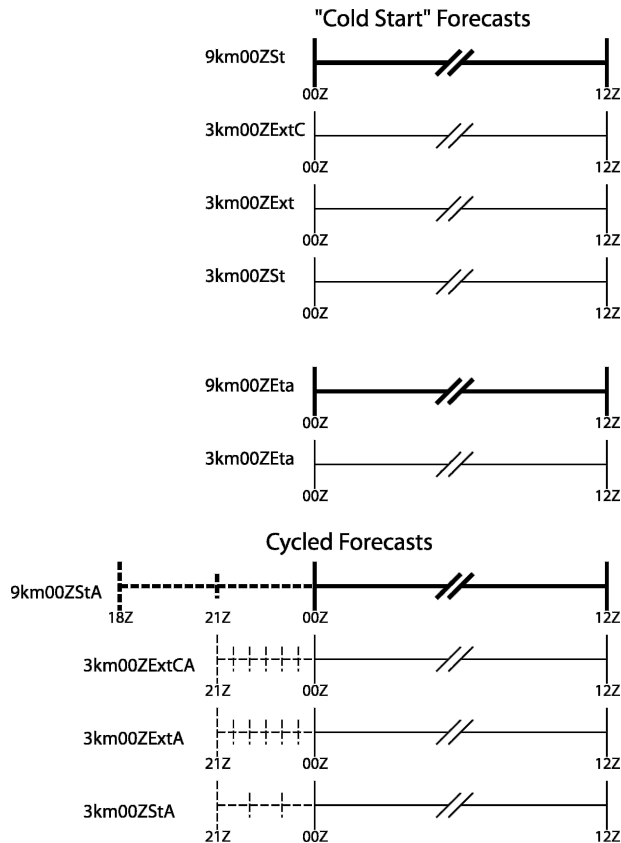


FIG. 4. Experiment configuration for the 3-km forecasts starting from 0000 UTC 16 Jun 2002. Solid horizontal lines and vertical ticks indicate forecast cycles, while dashed lines and ticks indicate assimilation cycles. Each 3-km forecast takes background fields and boundary conditions from the immediately preceding 9-km forecast.

b. Forecasts testing the impact of surface and upper-air data

Experiments 3km00ZExtC, 3km00ZExt, and 3km00ZSt (see Table 2) took initial and boundary conditions from experiment 9km00ZSt. In the case of 9km00ZEta, the initial condition was interpolated directly from the 0000 UTC 16 June 2002 National Centers for Environmental Prediction (NCEP) Eta real-time analysis, and the 9km00ZEta initial condition was then further interpolated to give the initial condition of 3km00ZEta. No additional analysis was performed for these “Eta” runs. For experiments whose names end with “St,” including 9km00ZSt and 3km00ZSt, data from standard observational networks, that is, surface aviation observations (SAO), raob, and WPDN are analyzed on their native grids. For the 3-km experiments ending with “Ext,” several additional surface data networks were included in the analysis. These are listed in Table 1. For the 1800 UTC experiments, the

configurations parallel those of 0000 UTC experiments, except for, of course, the initial time of the forecast.

For the finer-resolution 3-km grid, the analysis is performed using reduced spatial influence ranges to allow for increased detail, and the analysis of the coarser-resolution 9-km grid is used as the background. Such a “telescoping” procedure has a similar effect to performing multiple-analysis passes on a single high-resolution grid, but using increasingly smaller spatial influence ranges for the later passes while sometimes adding data from higher-resolution networks [see Brewster (1996) for a more detailed discussion on using the successive correction method with multiple passes]. This procedure is also followed by other sets of experiments that use different amounts of data. Details of the analysis configurations for the 9- and 3-km analyses are shown in Table 3. For the 3-km experiments using only standard data sources, only the first four analysis passes are performed. The somewhat large vertical influence ranges were chosen in order to allow information from surface measurements to be spread upward in the vertical. This was particularly important in the analysis of the surface cold pool. In several experiments, the analyzed cold pool extended farther south than that present in the background (Eta analysis). An effort was made to choose vertical influence ranges that would extend the analyzed cold pool upward from the surface to a depth comparable to the depth of the cold pool present in the background field. If too small a vertical influence radius is used for the surface data, the analyzed cold pool is too shallow and tends to be quickly removed by vertical diffusion in the model. Ideally, the vertical as well as the horizontal influence range should be determined by the locally determined flow-dependent background error covariances; unfortunately, such information is not generally available. Our semiempirical approach seems to work reasonably well here, although it should be stressed that there exists uncertainty with the choice of vertical and horizontal influence ranges.

c. Forecasts testing the use of a cloud analysis

Experiments 3km00ZExtC, 3km00ZExtCA, 3km00ZEtaC, 3km18ZExtC, 3km18ZExtCA, and 3km18ZEtaC (Table 2) all contained a cloud-analysis procedure incorporating NEXRAD level-II radar reflectivity data. Experiments 3km00ZExtCA and 3km18ZExtCA, which contained assimilation cycles over a 3-h period, will be discussed in the next section. Experiments 3km00ZExtC, 3km00ZEtaC, 3km18ZExtC, and 3km18ZEtaC are the same as 3km00ZExt, 3km00ZEta, 3km18ZExt, and 3km18ZEta, respectively, except for the inclusion of an additional cloud

TABLE 2. Details of the 9- and 3-km assimilation–forecast experiments, with the forecasts starting at 0000 UTC.

Expt	Description
9km00ZEta	Initial and boundary conditions interpolated from 0000 UTC 16 Jun 2002 Eta analysis.
9km00ZSt	Standard SAO, raob, and WPDN data analyzed at 0000 UTC on the 9-km grid using the 9km00ZEta initial fields as the background. Boundary conditions taken from the 0000 UTC Eta forecast fields.
9km00ZStA	Similar to 9km00ZSt, but with a 6-h assimilation cycle from 1800 UTC 15 Jun to 0000 UTC 16 Jun (3-h increments).
3km00ZEta	Initial conditions interpolated from 0000 UTC 16 Jun 2002 Eta analysis (via 9km00ZEta). Boundary conditions from 9km00ZEta forecast.
3km00ZSt	Standard SAO, raob, and WPDN data analyzed at 0000 UTC on 3-km grid using the analysis of 9km00ZSt as the background.
3km00ZStA	Same as 3km00ZSt, but with a 3-h assimilation cycle (1-h increments) from 2100 UTC 15 Jun to 0000 UTC 16 Jun. Background and boundary conditions from 9km00ZStA.
3km00ZExt	Same as 3km00ZSt, but additional extra surface data (listed in Table 1) are used in the initial analysis.
3km00ZExtC	Same as 3km00ZExt, but including an additional cloud analysis using NEXRAD level-II data.
3km00ZExtCA	Same as 3km00ZExtC, but with an assimilation cycle from 2100–0000 UTC. Additional surface data brought in every 30 min include OKMESO, WTXMN, ISFF, ARS, ARMS, ASOS, ABLE, NCAR, and ISS. Additional cloud analyses were performed every 30 min.

analysis for the initial condition. The purpose of 3km00ZEtaC and 3km18ZEtaC was to test the impact of the cloud analysis without the analysis of conventional data, in an effort to gauge the relative importance

of the cloud analysis versus the analysis of conventional data. Radar data from all reporting radars within the 3-km domain and their volume scans closest to the initial time were used. The 28 radars used are listed in

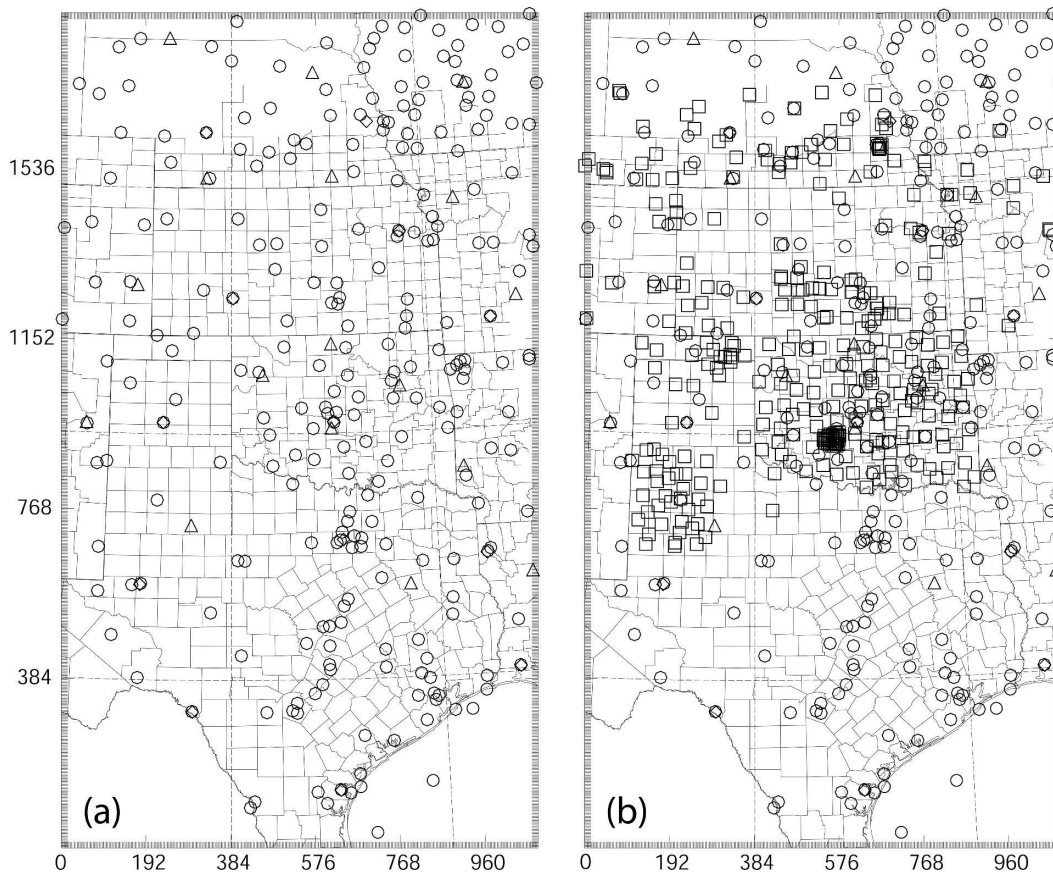


FIG. 5. Plot of locations of standard surface (circles), extra surface (squares), upper-air rawinsonde (diamonds), and upper-air profiler (triangles) stations in the 3-km domain as used in (a) standard data experiments and (b) extra data experiments.

TABLE 3. ADAS analysis configurations.

Analysis pass	Horizontal range (km)	Vertical range (m)	Data used
9-km analysis configuration			
1	500	750	raob, MDCRS, PRO
2	350	500	raob, MDCRS, PRO
3	150	500	raob, MDCRS, PRO, SAO, BUOY
3	100	500	SAO, BUOY
4	70	500	SAO, BUOY
3-km analysis configuration			
1	350	500	raob, PRO, MDCRS
2	160	500	raob, PRO, MDCRS
3	80	500	SAO, BUOY
4	60	500	SAO, BUOY
5	40	500	All extra networks (for Ext runs)
6	30	500	All extra networks (for Ext runs)

Table 4. Compared to a recent study by Hu et al. (2006a,b) that assimilates only one radar, the use of multiple radars is one of the special aspects of this study.

A brief discussion on the effect of the cloud-analysis scheme is in order. Brewster (2002) discusses recent upgrades to the ADAS cloud-analysis package involving, among others, the manner in which the potential temperature field is adjusted. The newer scheme used in this study adjusts the potential temperature in precipitation regions, based on the ingested reflectivity data, wherever there is an analyzed updraft, toward a moist adiabatic profile of a lifted cloud-base air parcel subject to dilution by mixing. Moisture and cloud microphysical fields are adjusted from the reflectivity based on the formulation of Smith et al. (1975). As examples, we show in Fig. 6 the vertical cross sections through the developing MCS of the analyses at the initial time, 0000 UTC 16 June 2002, from 3km00ZExt and 3km00ZExtC. The adjustment to the potential temperature and cloud water mixing ratio in cloudy regions due to the cloud analysis (right column) is evident. The vertical velocity is not directly affected by the cloud analysis at the initial time. However, as Fig. 7 shows, the model quickly responds to the cloud layer warming in 3km00ZExtC by spinning up a strong updraft within the cloud regions within 15 min of forecast while the vertical motion remains weak within this time period in 3km00ZExt. The potential temperature and cloud water fields for 3km00ZExtC (Figs. 7b,d) continue to show the maintenance of the convective clouds introduced by the cloud analysis, while no significant warming or cloud water has yet developed in 3km00ZExt (Figs. 7a,c). As is also found by Hu et al. (2006a), the

TABLE 4. WSR-88D sites in the 3-km domain.

Radar acronym	Radar names
KAMA	Amarillo, TX
KBRO	Brownsville, TX
KCYS	Cheyenne, WY
KDDC	Dodge City, KS
KDMX	Des Moines, IA
KEAX	Kansas City, KS
KEWX	Austin/San Antonio, TX
KFDR	Altus Air Force Base, OK
KFSD	Sioux Falls, SD
KFTG	Denver, CO
KFWS	Dallas/Fort Worth, TX
KGLD	Goodland, KS
KHGX	Houston/Galveston, TX
KICT	Wichita, KS
KINX	Tulsa, OK
KLBB	Lubbock, TX
KLNX	North Platte, NE
KLZK	Little Rock, AR
KMAF	Midland/Odessa, TX
KOAX	Omaha, NE
KPUX	Pueblo, CO
KSGF	Springfield, MO
KSHV	Shreveport, LA
KSRX	Western Arkansas/Fort Smith, AR
KTLX	Oklahoma City, OK
KTWX	Topeka, KS
KUEX	Hastings, NE
KVNX	Vance Air Force Base, OK

adjustment to the thermal field plays an important role in the cloud initialization, perhaps more than the analysis of the cloud fields themselves. When enough thermal buoyancy is present in the initial conditions because of the thermal adjustment, it can be expected that the cloud fields will be built up quickly in the model as the nearly saturated buoyant air begins to rise and water vapor condenses into cloud water.

d. Forecasts with intermittent data assimilation cycles

Finally, several forecasts, with names ending with "A," designed to test the impact of assimilating data over a period of time, via intermittent assimilation cycles, were performed. When the assimilation cycles are included, they are performed on both 9- and 3-km grids, with the 9-km runs again primarily serving to provide the boundary conditions for the corresponding 3-km runs. Experiments 9km18ZStA and 9km00ZStA both contained 6-h assimilation cycles with 3-h increments prior to the initial times of forecast at 1800 and 0000 UTC, respectively. Within the assimilation windows, these two runs used the 1200 and 1800 UTC Eta analysis and 3-h forecast, respectively, for the initial

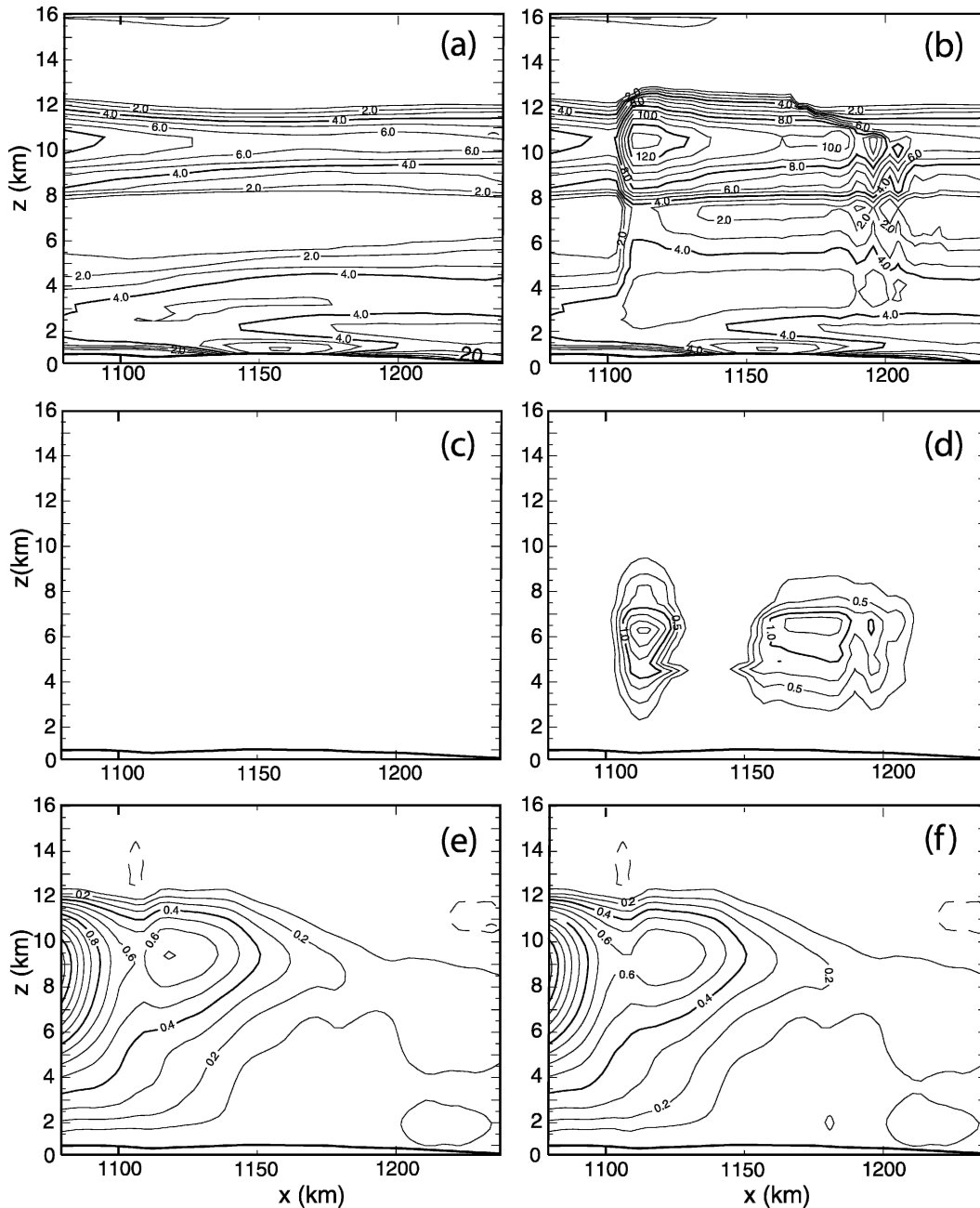


FIG. 6. Vertical cross section through the developing MCS as revealed by the initial analyses at 0000 UTC 16 Jun 2002: (a) perturbation potential temperature in increments of 1 K, (c) cloud water mixing ratio in increments of 0.25 g kg^{-1} , and (e) vertical velocity contoured in increments of 0.1 m s^{-1} for 3km00ZExt without cloud analysis. (b), (d), (f) The corresponding fields from the analysis of 3km00ZExtC.

analysis background and the boundary conditions. At 1800 and 0000 UTC, the end of the assimilation window for the two cases, respectively, Eta analyses were used to provide the lateral boundary condition. In other words, analysis boundary conditions from the available Eta analyses were used when possible during the assimilation windows. For the final forecast cycle of

9km18ZStA (9km00ZStA), the 1800 UTC (0000 UTC) Eta forecasts were used as the boundary conditions. The 3-km “cycled” runs were nested inside the corresponding 9-km runs, using 3-h assimilation windows with 30-min intervals, except for the St runs, which used 1-h intervals because of the lower temporal frequency of data (see again Fig. 4). For the assimilation cycles,

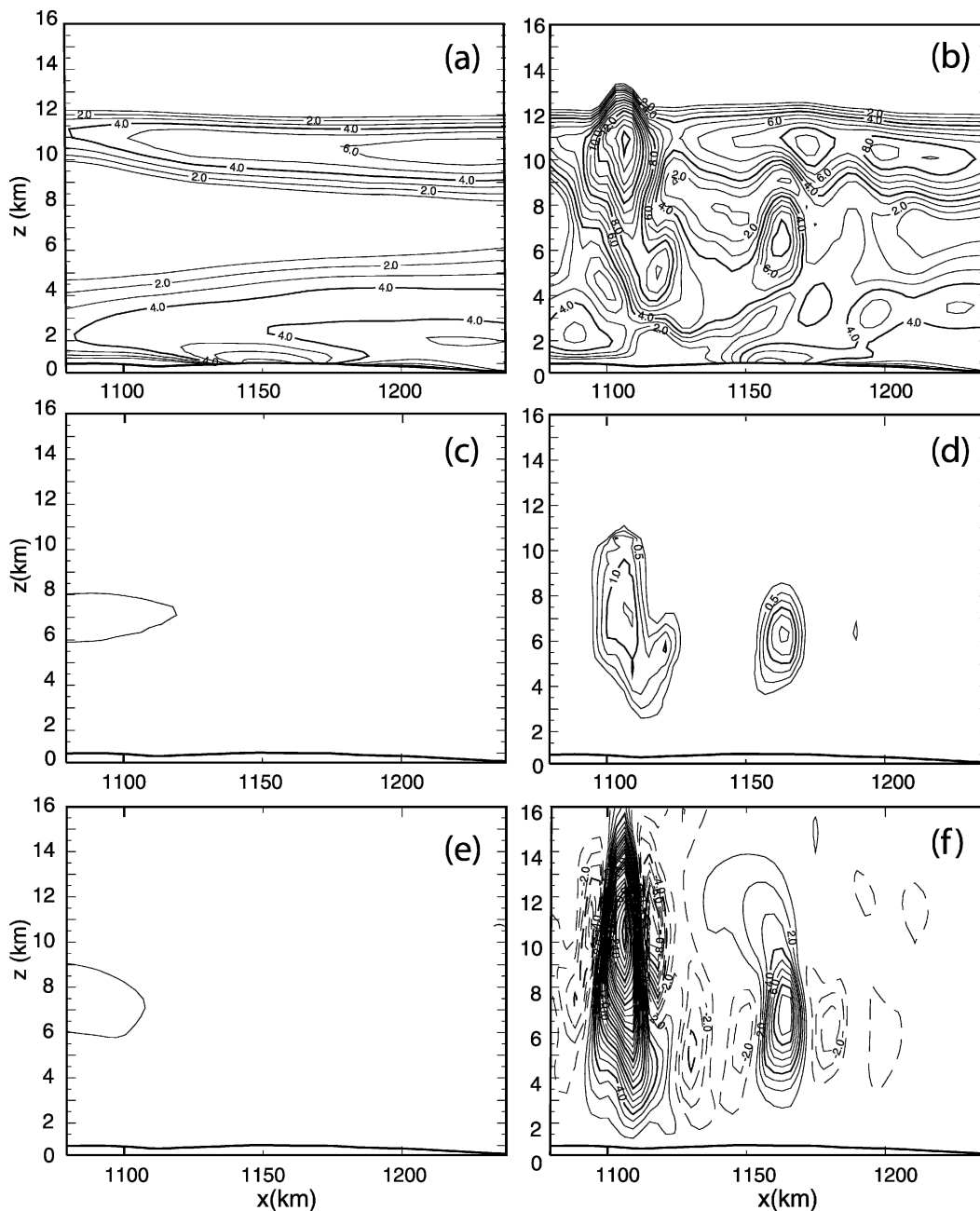


FIG. 7. As in Fig. 6, but for 15 min into the forecast. In (e) and (f), the vertical velocity w is contoured in 1.0 m s^{-1} increments.

additional surface data were brought in via an ADAS analysis and the level-II radar data from the closest volume scans were brought in via the cloud analysis. The frequent assimilation cycles are expected to help build up and maintain the MCS in the model.

e. Verification procedures

Verification of numerical forecasts of small-scale convective systems is difficult because of the spatial and

temporal intermittency of such systems and the inherent predictability limit of individual convective elements. Traditional skill scores, such as the equitable threat score (ETS), originally designed for large-scale forecast fields such as coarse-grid forecasts of accumulated precipitation, have limited utility when applied to small-scale convective systems (Baldwin et al. 2002). The difficulties arise because small-scale convective systems such as the bow echo in this study tend to be

discrete, high-amplitude events, and even a small position error due to, for example, the errors in the prediction of direction or speed of propagation can result in very low skill scores, even when the structure of discrete systems is captured by the prediction model rather well. Subjective evaluations of the prediction fields remain important parts of forecast verification at the convective scales. Some recent research on the mesoscale and small-scale model verification has focused on pattern and/or feature identification techniques that attempt to automate or make objective the subjective evaluations (e.g., Ebert and McBride 2000; Baldwin et al. 2001, 2002; Nachamkin 2004).

With the above considerations in mind, our verification involves the use of both subjective and qualitative evaluations of the various forecasts against observations, and a quantitative approach involving the calculation of the ETS. We will discuss the results of both the qualitative and quantitative verifications of primarily the forecast radar reflectivity fields because radar reflectivity is a quantity that is most directly observed at the convective scale.

The ETS calculations were performed on the model grid for the fields of composite radar reflectivity, which is a 2D field defined as the maximum radar reflectivity in a vertical column. The ETS, also known as the Gilbert skill score (Schaefer 1990), is a widely used verification statistic in meteorology and is a measure of the accuracy of the forecast in predicting a certain forecast event, which in this case is prediction at a given location and time at or above a certain value of composite reflectivity. It is given by $ETS = (H - H_R)(H + M + F - H_R)^{-1}$, where H is the number of hits, that is, the number of correctly forecasted events; M is the number of misses, that is, events that were observed but not forecasted; F is the number of false alarms, events that were forecasted but not observed; and H_R is the number of correctly forecasted events expected from random chance and is given by $H_R = (H + M)(H + F)T^{-1}$, where T is the total number of points in the verification domain. ETS is most often used for precipitation verification in meteorology; we choose the composite reflectivity as the verification field, however, for this study because it, in addition to the reasons mentioned earlier, is a field that can be easily derived from the level-II data of multiple NEXRAD radars, and for the model forecast it can be derived from the model hydrometeor fields (with approximations). As sequences of instantaneous fields, they contain a great deal of information about the structure, intensity, and evolution of convective systems such as the MCS in this study. On the other hand, at a resolution of a few-

kilometers, the available precipitation data are usually derived from radar reflectivity fields, and the derivation often involves many assumptions, hence introducing many more uncertainties than with the reflectivity data. Furthermore, accumulated precipitation data do not have the temporal precision offered by instantaneous reflectivity data.

To calculate the observed composite reflectivity, the raw level-II data from multiple radars were first remapped from the radar coordinates to the ARPS grid, and the maximum value of reflectivity for each vertical column was determined. Similarly, the forecast composite reflectivity was determined from the model gridpoint values of reflectivity calculated from the model hydrometeor fields. The reflectivity formulations for different hydrometeors can be found in Tong and Xue (2005, 1791–1792) and are mainly based on Smith et al. (1975). Once the composite reflectivity fields are determined, the ETS can be readily calculated.

We chose to calculate the ETSs at various times on both the “raw” forecast composite reflectivity fields, and on these fields after they had been shifted in the horizontal to line up the leading edge of the forecast MCS with that of the observations. The goal of this phase shifting is to obtain the maximum possible threat scores that reflect more of the accuracy of the predicted *structure* of the MCS. When working well, the amount of spatial shift that maximizes the threat score also tells us, in an objective way, about the amount of position error. The phase-shifting technique used here is similar to the contiguous rain area verification technique of Ebert and McBride (2000), with the main differences being the use of the composite reflectivity field as the field for which the horizontal translation is performed instead of the rain rate field, and the use of the ETS as the “best fit” statistic instead of the total squared error or pattern correlation coefficient.

The phase-shifting algorithm works by shifting the forecast grid relative to the original grid in increments of one grid interval at a time in all possible horizontal directions until the maximum ETS is found. The 50-dBZ reflectivity threshold is chosen for determining the optimal spatial shifts, as the 50-dBZ contour in this case is found to best represent the outline of the leading convective region of the MCS in both the forecasts and observations, for most of the time periods examined. In other cases, a different threshold might be more suitable. The phase-shifting algorithm as described would only work well when the structure of convective system as revealed by the composite reflectivity is reasonably well predicted. In our case, the detailed structure of the

forecasted MCS differs appreciably from that of the observed at times, so that the ETS-maximizing phase-shifting approach does not produce a satisfactory result for all times and for all forecasts. The problem is exacerbated by both the high bias in areal coverage of the higher values of forecast reflectivity, and the low bias in areal coverage and more bowed structure of the overall forecast MCS.

For these reasons, an option is provided in which a subjectively determined amount of shift is used as the starting point for the subsequent objective ETS-maximizing shift that is limited to a relatively small search area around this starting point. This technique is found to work better for most of the forecast times and is therefore used throughout this study. In addition, to ensure fair comparisons among all forecasts, we calculate our ETS within a common domain that excludes the near-boundary regions not covered by some of the shifted grids.

In this study, the calculations of ETS for composite reflectivity are performed hourly for a 12-h period from 0000 UTC 16 June to 1200 UTC 16 June for the 0000 UTC forecasts, and from 1800 UTC 15 June to 0600 UTC 16 June for the 1800 UTC forecasts. Table 4 shows a list of the 28 radars in the 3-km domain that are used for the analysis as well as for verification. In the case of one radar site, KHGX, level-II data were not available between 0600 and 1200 UTC, the last 6 h of the forecast period. For this period, level-III data were used to fill the gap.

5. Results

a. Model spinup of the MCS

In most forecasts, a well-defined, bow-shaped MCS developed and propagated south-southeastward in a similar manner as the observed MCS. Figure 8 shows a comparison of the observed composite reflectivity fields for 0000, 0600, and 1200 UTC and the corresponding model fields from experiment 3km00ZExtC, which included extra data from a number of special networks as well as radar data through the cloud analysis. At 0000 UTC, the two are essentially the same due to the cloud analysis. The structure and position of the MCS are captured by the model to a remarkable degree during the 12-h forecast. While the MCS also developed in other forecasts, there are significant differences in the position, size, and shape of the forecast MCS. In particular, there is in general a significant time delay that is reflected in the position error in the forecasts that did not include a cloud analysis. Such varying spinup times of the system across the forecasts appear to account for most of the differences. Figure 9 shows

the observed and forecast composite reflectivity fields from 3km00ZExt and 3km00ZExtC at 1 and 2 h into the forecast. In the initial condition (not shown), the 3km00ZExt contains no nonzero reflectivity because of the lack of cloud initialization and the reflectivity associated with the MCS did not begin to develop until about 1 h (Fig. 9c). In 3km00ZExtC, because of the cloud analysis, an identifiable bow-shape structure is fully developed by 1 h (Fig. 9e) that propagated southward by about 50 km in the next hour (Fig. 9f), so that its southward progress is closer to that of the observed (Fig. 9b) than in 3km00ZExt (Fig. 9d). As a result, the convective system in 3km00ZExt as well as in other forecasts that do not include a cloud analysis, including 3km00ZSt and 3km00ZEta (not shown), lags in time and space compared with the observed system and that forecasted by 3km00ZExtC. In general, this position lag is also true of the 1800 UTC forecasts.

We examine how soon convection develops in the model after the initial time; we plot in Fig. 10 the time series of the domainwide maximum vertical velocities for the 0000 UTC 3-km cold start forecasts. The cycled 3-km forecasts, as a result of the assimilation window, all were able to spin up significant convective updrafts by the initial forecast time (0000 UTC) and are not shown here. It is clear from the figure that intense updrafts develop almost immediately in the forecasts (3km00ZExtC and 3km00ZEtaC) that included a cloud analysis in the initial condition, while it took almost 2 h for the updrafts to reach their initial peak values in 3km00ZExt and 3km00ZSt, which included additional but not radar data in the initial conditions. It took even longer, in fact almost 3 h, for the same to be reached in 3km00ZEta, which started from the interpolated Eta analysis. Figure 11 shows the domainwide maximum vertical velocities for the 1800 UTC “cold start” forecasts. The results are similar to those of the 0000 UTC experiments and indicate that the general effect on the spinup times of adding an additional data analysis does not appear to be sensitive to the time of initial condition. These results also indicate that the inclusion of additional data in the initial condition, even without cloud analysis, reduces the spinup time of the MCS (more on this later).

It should be pointed out that the standard data sources used in this study were probably already included in the 1800 and 0000 UTC Eta analyses. However, the gridded Eta analysis that was used in this study was at 40-km horizontal resolution and had already gone through interpolations to the pressure surfaces from the original model grid. Our multipass analysis on the native ARPS grid at up to 3-km resolution and using increasingly smaller influence ranges

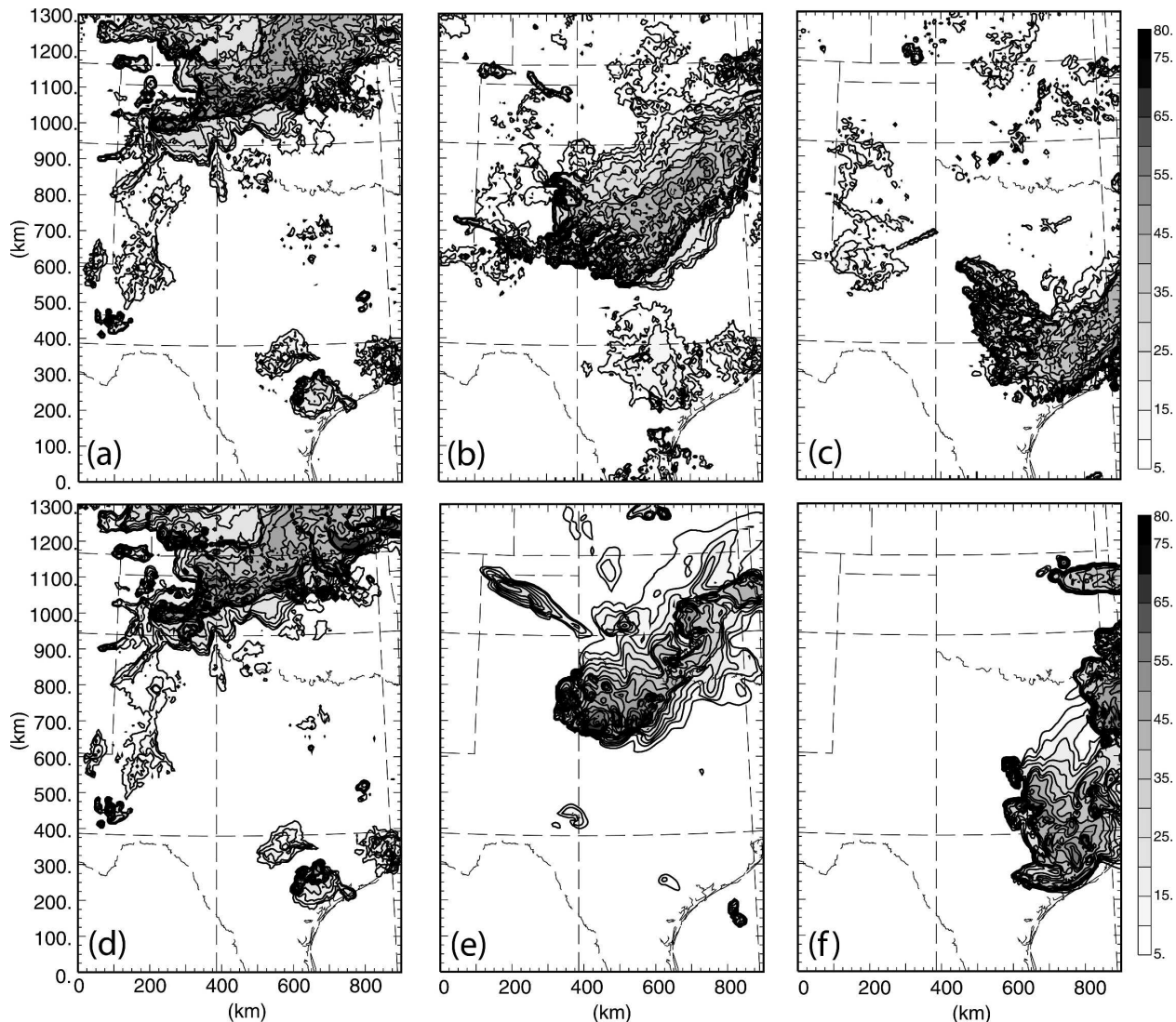


FIG. 8. (top) Observed and (bottom) 3km00ZExtC forecast composite reflectivity for (left) 0, (middle) 6, and (right) 12 h into the forecast, corresponding to 0000, 0600, and 1200 UTC 16 Jun 2002, respectively. Contour interval is 5 dBZ, and only a portion of the full 3-km domain is shown.

should allow for more finescale structures present in the data to be retained. This is, we believe, the reason for the improvement of 3km00ZSt and 3km18ZSt over 3km00ZEta and 3km18ZEta, respectively, and this will be discussed further in section 6.

b. Phase errors in the MCS forecasts

We assess the amount of position or phase error in each of the 0000 UTC 3-km forecasts; we plot in Fig. 12 the observed (gray) and forecast (black) 45- and 50-dBZ composite reflectivity contours valid at 0600 UTC 16 June 2002, or 6 h into the forecast. The vectors of spatial shift as derived from the phase-shifting algorithm are also plotted for the forecasts. As can be seen,

the shift vectors at this time for 3km00ZSt and 3km00ZExt are very similar, while that of 3km00ZEta is the largest. These results indicate that the additional analysis on top of the Eta analysis is able to improve the position forecast of the MCS. The three forecasts that included a cloud analysis in the initial conditions show smaller position errors, with 3km00ZExtCA having the smallest position error of all the forecasts at this time. Also evident is the improved shape and size of the MCS in each of the cloud-analysis runs (Figs. 12b,e,h) compared with the non-cloud-analysis runs. The forecasts with assimilation cycles (Figs. 12f,g,h) also show reduced position errors, comparable in magnitude to position errors of the cold start cloud-analysis forecasts.

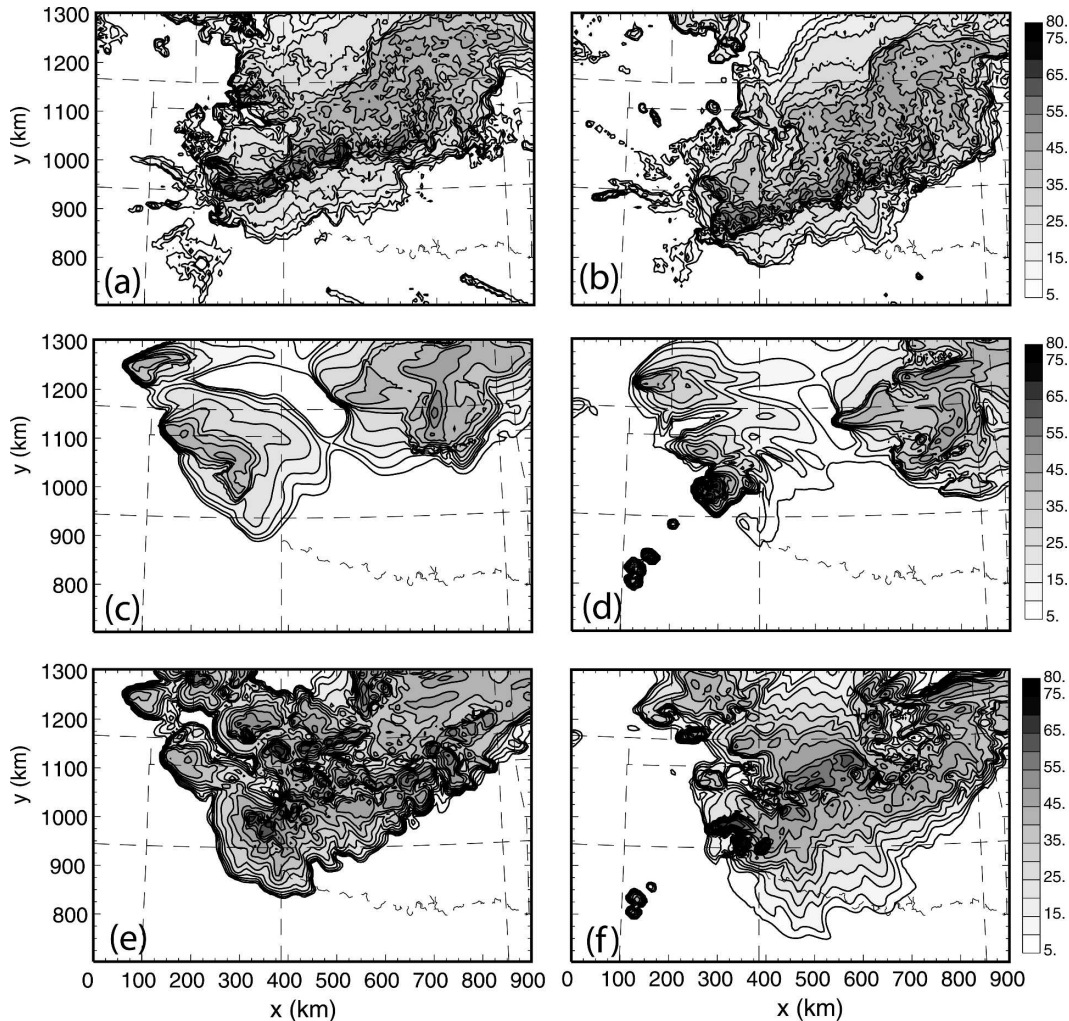


FIG. 9. (top) Observed, (middle) 3km00ZExt forecast, and (bottom) 3km00ZExtC forecast composite reflectivity for (left) 1 and (right) 2 h into the forecast, corresponding to 0100 and 0200 UTC 16 Jun 2002, respectively. Contour interval is 5 dBZ.

Figure 13 shows the position errors derived from the phase-shifting algorithm for each of the 0000 UTC forecasts for the period between 0000 and 1200 UTC. From this figure, it is clear that the forecasts including the cloud analysis demonstrate significantly smaller position errors throughout the period. In the following discussion, all averages, maxima, and minima are taken between 0200 and 1200 UTC, because the MCS was still spinning up during the first 2 h of forecast for some of the experiments. For example, in the case of 3km00ZExt, the average position error of the MCS from these calculations was approximately 177 km, while for 3km00ZExtC, it was 76 km, an improvement of approximately 57%. Even for 3km00ZExtC, which contained no other data analysis other than the cloud analysis at the initial time, the position errors are re-

markably small, with an average position error of 81 km, close to that of 3km00ZExtC. The maximum position error for 3km00ZExt was 212 km, and the minimum was 126 km, while the corresponding values for 3km00ZExtC are 109 and 23 km, respectively. Experiment 3km00Zeta showed overall the largest position errors in the first half of the forecast, but the forecast, interestingly, began to improve markedly in the latter half of the forecast period, so that its average position error of 174 km was actually better than the 190 km of 3km00ZSt. This appears to be the result of an improved organization (not shown) of the MCS in 3km00Zeta after about 6 h such that the MCS in the model began to accelerate and “catch up” with the observed system, while the structure of the MCS in 3km00ZSt deteriorated during this same time period. As Fig. 13 shows,

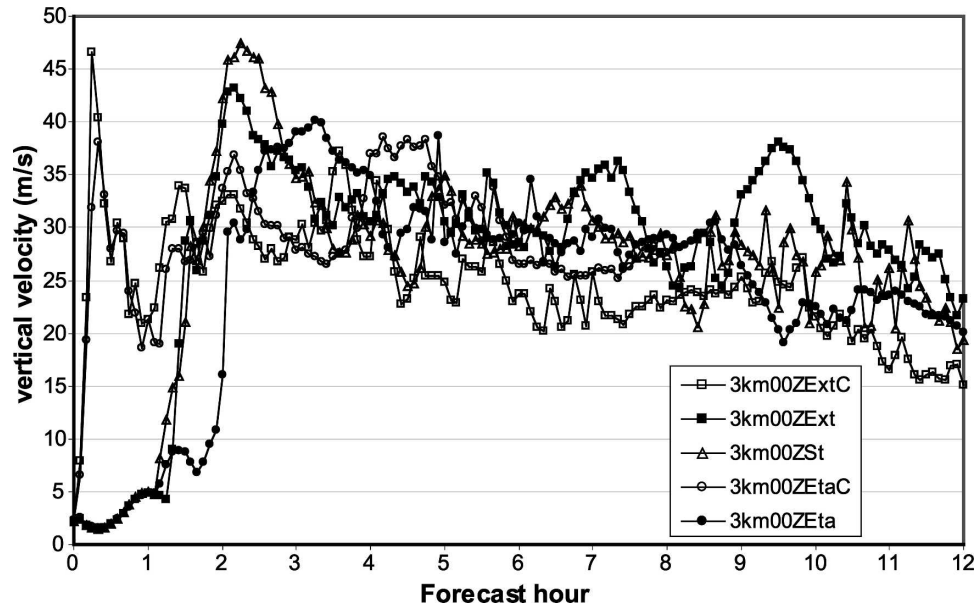


FIG. 10. Maximum upward vertical velocity vs time for the 0000 UTC 3-km forecasts.

3km00ZSt had the worst position errors of all the forecasts during the latter half of the forecast period. It is not at all obvious why 3km00ZSt should be worse than 3km00ZEta; a likely reason is the highly nonlinear nature of the prediction. However, in general, the more data that were used in the initial conditions, the lower the position errors. Furthermore, the use of a 3-h assimilation window prior to the 0000 UTC start time also served to improve the position forecast of the MCS, and

even more so when cloud analyses are included in the cycles, so that 3km00ZExtCA had the overall best position forecast, with an average position error of only 67 km.

c. ETS for composite reflectivity

Figure 14 shows the raw (unshifted) and phase-shifted hourly ETS scores for reflectivity thresholds of 15, 30, and 45 dBZ for each of the 0000 UTC 3-km

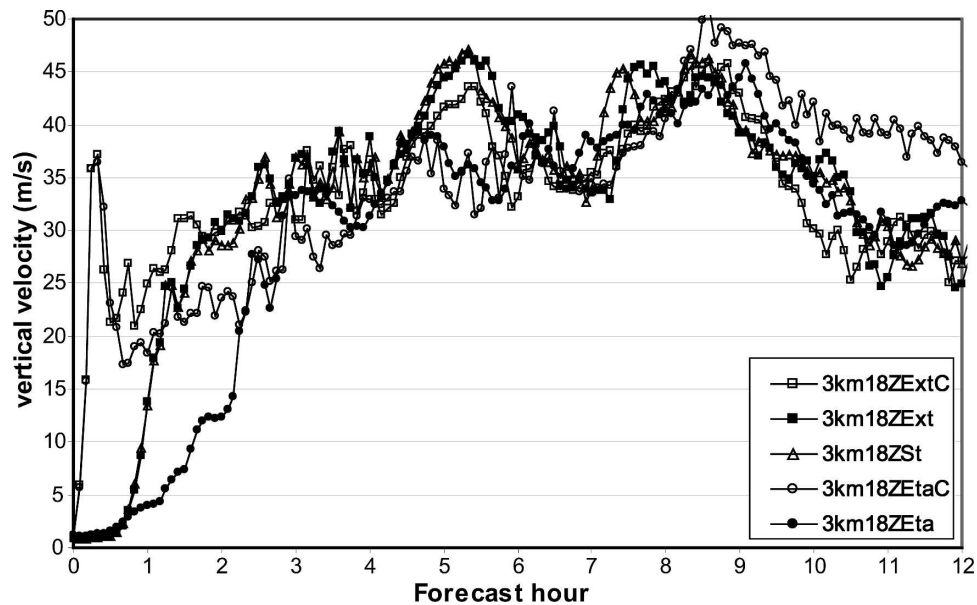


FIG. 11. As in Fig. 10, but for the 1800 UTC forecasts.

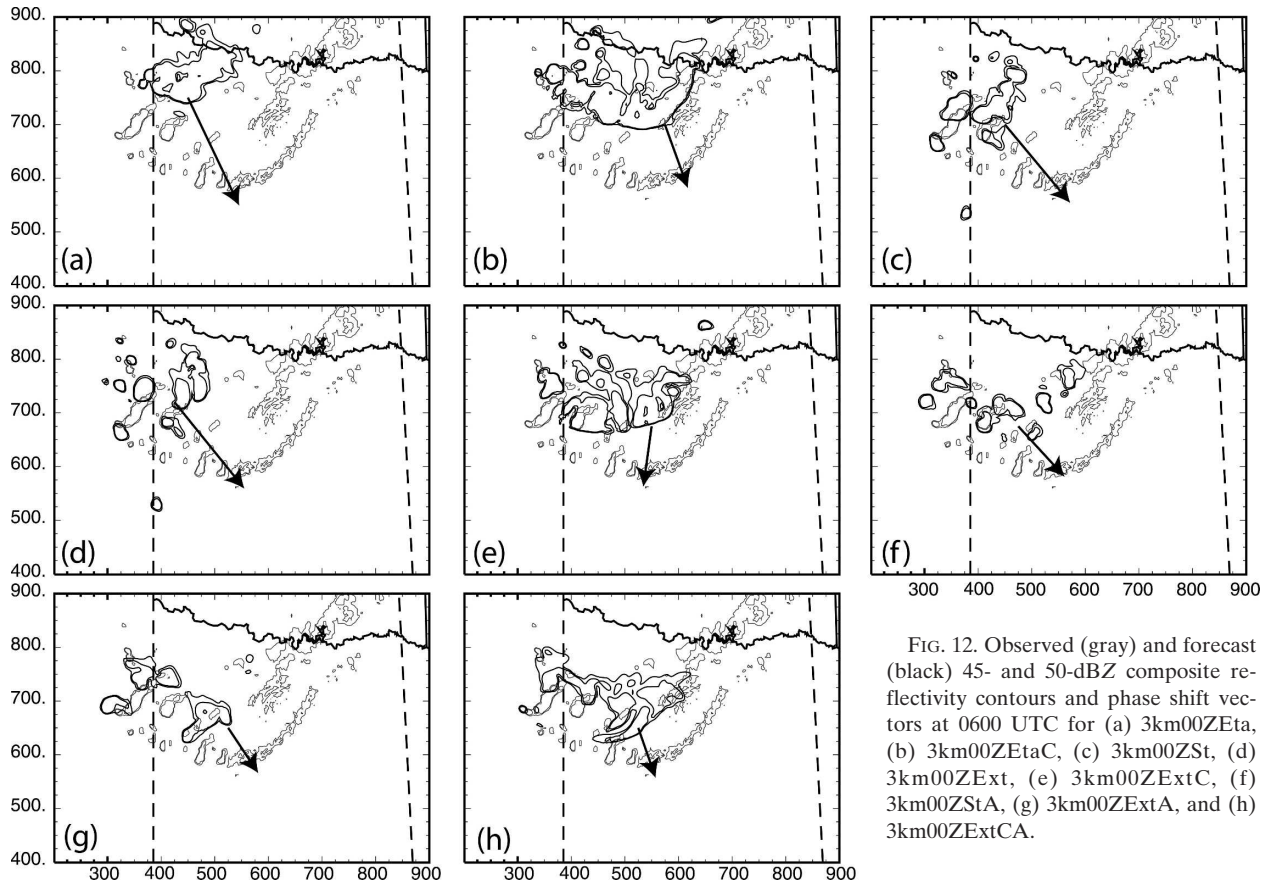


FIG. 12. Observed (gray) and forecast (black) 45- and 50-dBZ composite reflectivity contours and phase shift vectors at 0600 UTC for (a) 3km00ZEta, (b) 3km00ZEtaC, (c) 3km00ZSt, (d) 3km00ZExt, (e) 3km00ZExtC, (f) 3km00ZStA, (g) 3km00ZExtA, and (h) 3km00ZExtCA.

forecasts. The calculations were performed on the common grid as determined by the maximum phase shift of each time. The raw ETS scores calculated on the full 3-km domain (not shown) are, in general, somewhat

higher than those in Fig. 14. As can be seen from the figure, for each threshold and throughout most of the forecast, the three experiments that included a cloud analysis, 3km00ZExtC, 3km00ZEtaC, and 3km00ZExtCA,

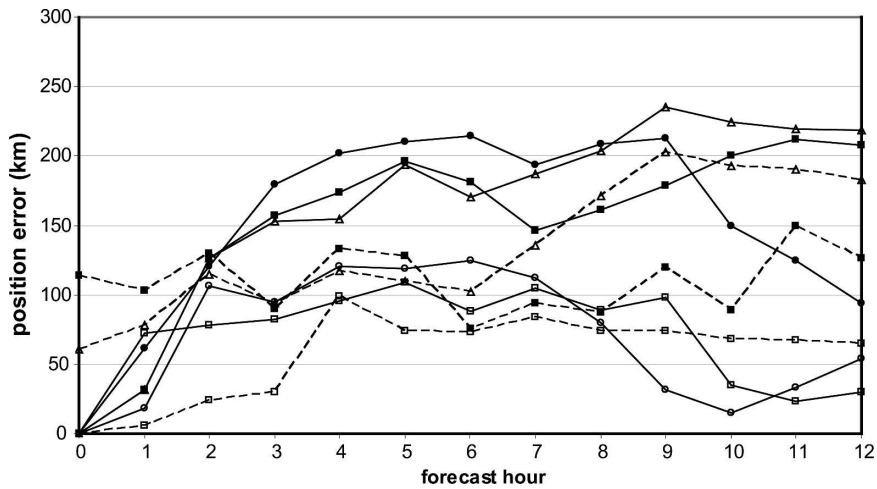


FIG. 13. Position errors for the 3-km forecasts derived from the phase-shifting algorithm. Dashed lines with open squares denote 3km00ZExtCA, dashed lines with closed squares denote 3km00ZExtA, and dashed lines with open triangles denote 3km00ZStA. Other line markers are as in Fig. 10.

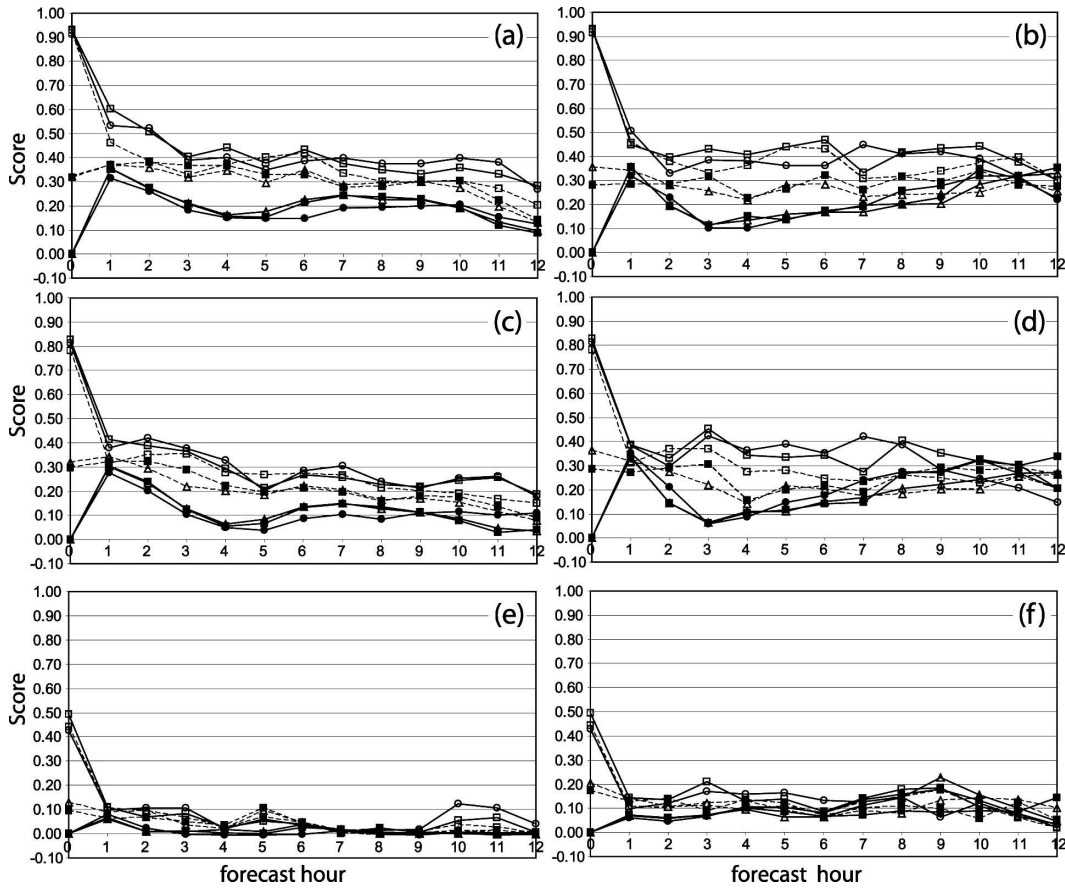


FIG. 14. (left) Raw and (right) phase-shifted ETS for thresholds of (top) 15, (middle) 30, and (bottom) 45 dBZ for the 0000 UTC 3-km forecasts. The line markers are as in Fig. 13.

had significantly higher ETS. This is true even though, again, the 3km00ZetaC contained no other data, except for the radar data. Thus, it appears from these results that the cloud analysis overwhelms any other potential improvement from assimilating more conventional data sources in the initial conditions. Also apparent from this figure is the improvement in both raw and phase-shifted scores for forecasts that included a 3-h assimilation cycle prior to the 0000 UTC initial time over those of their noncycled counterparts, with the sole exception of 3km00ZExtCA, which had consistently lower scores than 3km00ZExtC. An examination of the reflectivity fields during the forecast period (not shown) for these two forecasts reveals that the frequent (every 30 min) application of the cloud analysis during the 3-h assimilation window may have resulted in over-adjustment of the thermodynamic profiles in the precipitation regions, resulting in too many updrafts and nonlinear interactions that actually made the prediction of the MCS structure slightly worse in 3km00ZExtCA than in 3km00ZExtC. This result is possible because the cloud analysis at each time does not effectively re-

move spurious convection that may have developed in the previous 30-min forecast cycle, but merely adjusts cloud and thermodynamic fields based on the observed reflectivity field at each time, and removing only the hydrometeor fields in regions outside the observed reflectivity but leaving alone the thermal and wind perturbations in those regions. This suggests that the application of a cloud analysis in the context of frequent assimilation cycles should be used with caution, or more sophisticated techniques, including those that more effectively remove spurious convection, should be used in conjunction with the cloud analysis. Nevertheless, as mentioned previously, the use of the assimilation cycles still resulted in a superior prediction of the *position* of the MCS, even though the ETSS do not reflect an improvement in either the raw or phase-shifted versions.

Interestingly, rather than decreasing with time, as might be expected, the ETS at thresholds of 15 and 30 dBZ for all forecasts that did not include a cloud analysis remained relatively steady or even increased slightly at times during the forecast period. The cloud-analysis

forecasts, on the other hand, showed generally decreasing scores from initially high values, so that the scores from all forecasts tended to converge toward the end of the period (1200 UTC). The explanation for this behavior is that, in the case of the non-cloud-analysis runs, the MCS got spun up and became progressively more organized in the model with time, resulting in the steady or most often the slightly increased scores. Such increase in scores during the latter half of the forecast period is more pronounced in the shift scores, especially in those for 30 dBZ (Fig. 14d), which indicates strongly the development and organization of the MCS in the forecasts, but the time lag and position errors prevented the achievement of high raw threat scores (Fig. 14c). In the cases of the cloud-analysis runs, the MCS is analyzed in the initial condition; its prediction gradually degrades with time, as one would expect of any properly analyzed system. It is interesting to point out that the raw scores of the cloud-analysis runs remained higher than all other runs that did not include a cloud analysis, for nearly the entire period shown, and furthermore, this advantage is maintained even in terms of the shifted scores for nearly all times. Still, there is a tendency for the scores of the cloud-analysis cases to approach those of the non-cloud-analysis cases, indicating the gradual loss of impact of the initial cloud analysis.

At a threshold of 45 dBZ, the raw ETSs (Fig. 14e) show virtually no skill for the non-cloud-analysis forecasts, while forecasts with a cloud analysis exhibit low but positive skills. The main reason for the low or even zero scores is because of the very limited spatial coverage by the high reflectivity regions; therefore the overlap of the predicted and observed regions is harder to achieve.

The phase-shifted ETSs (Fig. 14, right column) for the various forecasts are qualitatively similar to their raw counterparts, except that, as expected, the scores are generally higher, particularly for the higher thresholds of reflectivity, and for the middle and later portions of the forecast. This is to be expected, because of the phase-shifting algorithm attempting to match up the higher reflectivity cores of the forecast and observed MCS. For the 45-dBZ threshold, the scores for the non-cloud-analysis runs are increased by the shifting from essentially zero to values at or above 0.10 for most of the times, and the improvement for the 30-dBZ threshold is equally dramatic, especially toward the end of the period. The fact that the shifted scores and the raw ETSs are quite different suggests the limitations of examining the raw ETS alone; it does not tell us if the low score is due to the model's failure to forecast the convective system altogether, or a result of possible posi-

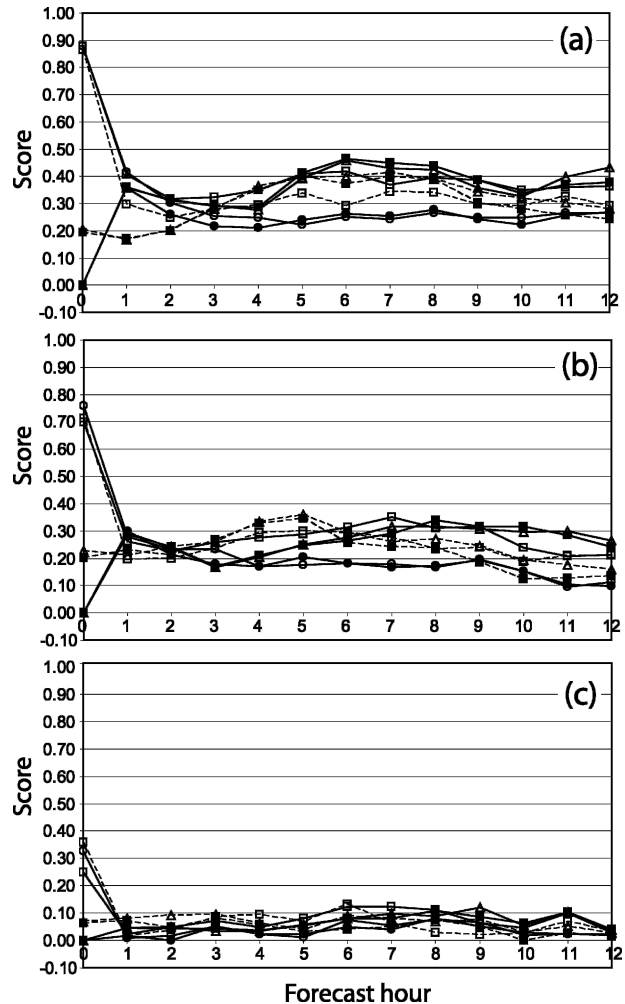


FIG. 15. Raw ETSs for (a) 15-, (b) 30-, and (c) 45-dBZ thresholds for the 1800 UTC forecasts. Line markers are the same as the corresponding 0000 UTC forecasts.

tion errors of perhaps an otherwise reasonably predicted system in terms of its structure. Examining both raw and shifted scores, as well as the amount of shift needed to obtain the maximized scores, is clearly revealing.

An attempt was made to perform phase shifting for the 1800 UTC set of forecasts as well. However, the MCS was going through an organization phase, as previously discussed, during the first 5–6 h of the forecast period in the observations, and in some of the forecasts took even longer than this to organize into a well-defined bow echo. As such, it was difficult to match, for phase-shifting purposes, the developing system with the observed one through most of the forecast period. Therefore, we present in Fig. 15 only the raw ETS scores for the 1800 UTC forecasts, for comparison with the raw ETSs for the 0000 UTC runs in Fig. 14. The

TABLE 5. Average raw and shifted ETSs from 0200 through 1200 UTC for the 0000 UTC 3-km forecasts.

Forecast	15 dBZ		30 dBZ		45 dBZ	
	Raw	Shifted	Raw	Shifted	Raw	Shifted
3km00ZEta	0.18	0.20	0.10	0.21	0.0020	0.10
3km00ZEtaC	0.39	0.37	0.28	0.32	0.058	0.12
3km00ZSt	0.20	0.21	0.11	0.18	0.010	0.10
3km00ZExt	0.19	0.23	0.11	0.20	0.0059	0.086
3km00ZExtC	0.38	0.40	0.27	0.33	0.039	0.13
3km00ZStA	0.29	0.26	0.18	0.21	0.029	0.11
3km00ZExtA	0.30	0.29	0.20	0.25	0.029	0.10
3km00ZExtCA	0.33	0.36	0.25	0.27	0.038	0.10

scores for each time were calculated on the same domains as the corresponding scores for the 0000 UTC runs, to facilitate a fair comparison.

As can be seen, there are some notable differences in the behavior of the ETS scores for the 1800 UTC forecasts as compared with the 0000 UTC forecasts. The main differences are the lack of improvement in the scores for the cloud-analysis runs (3km18ZExtC, 3km18ZExtCA, and 3km18ZEtaC). In each of these cases, the scores are very similar to their non-cloud-analysis counterparts (3km18ZExt, 3km18ZExtA, and 3km18ZEta) for each threshold shown in Fig. 15. These results indicate that the cloud analysis provides little benefit when an organized convective system is not present in the initial conditions, as was the case at 1800 UTC 15 June 2002. Also of note from the scores is the lack of any significant improvement in the forecast when assimilation cycles are used (dashed lines). (Recall that for the 1800 UTC forecasts, the assimilation cycles were every 30 min between 1500 and 1800 UTC, at a time when the MCS had yet to even begin to develop). In fact, in some cases, particularly for the 15-dBZ threshold (Fig. 15a), the assimilation cycle runs actually have worse scores than their cold start counterparts, even though they start at the initial time with nonzero scores. Taken together, these results suggest that the presence of an organizing or organized MCS in the initial conditions and/or assimilation window helps create and maintain the positive impact of assimilation cycles or cloud analyses on the subsequent model forecast. Otherwise, the impact is much less clear. This behavior may be partly due to the limitation of the current assimilation procedure (the analysis produced is not entirely balanced or consistent with the model dynamics and physics) and partly due to the predictability limit of the convective system (the benefit of analyzing convective cells or systems tends to be lost beyond their life cycle). Nevertheless, the impact of an additional data analysis on the high-resolution grid can still be seen in these scores, as for all thresholds, the scores for experi-

ments 3km18ZEta and 3km18ZEtaC are significantly lower for most of the forecast period than those of other experiments.

In Table 5 we summarize the average (taken between 0200 and 1200 UTC) raw and shifted ETSs for each of the 0000 UTC 3-km forecasts. Among the cold start forecasts that did not include a cloud analysis, no forecast in particular appears to be better than the other based on these scores alone, with both the raw and phase-shifted scores being very similar to each other. The cycled non-cloud-analysis runs, 3km00ZStA and 3km00ZExtA, both had average raw ETSs nearly twice as high as their noncycled counterparts, 3km00ZSt and 3km00ZExt, for the 15- and 30-dBZ thresholds, with an order of magnitude improvement in the scores for the 45-dBZ threshold; the average phase-shifted scores for these thresholds showed less of an improvement, but were still higher, suggesting that, at least in this case, the assimilation cycles improved both the position and structure forecasts of the MCS. The scores of 3km00ZExtC, either raw or shifted, are higher for all thresholds; they are near 0.4 for the 15-dBZ threshold, and near 0.3 for the 30-dBZ threshold, which can be considered very good considering that they are for instantaneous fields at the convective scale, and calculated on a high-resolution grid.

The average scores suggest that the additional surface data networks used in the initial conditions of 3km00ZExt did little to improve the forecast of the MCS over that using the standard networks as in 3km00ZSt, at least as far as the ETSs show. However, as mentioned previously, the additional data analysis was able to reduce the spinup time of the MCS, and thereby lower the position error of the forecast MCS, as will be discussed in more detail in the next section.

6. Further discussion on the data impact

In the previous section, we presented results from a quantitative analysis of the 3-km forecasts of an MCS.

It was shown that the analysis of the spin up of the MCS updrafts, the phase (position) errors, and the evaluation of raw and shifted ETSs for composite reflectivity all indicate a significant improvement in the forecast when a cloud analysis is performed for the initial conditions in the 0000 UTC forecasts. The impact of other data sources is present but much less obvious. Other earlier work has also demonstrated, to varying degrees, the positive impact of the use of a cloud-analysis procedure. Souto et al. (2003) reported a modest improvement in the forecast of precipitation patterns and amounts in northwest Spain when a simple cloud-analysis-like procedure that does not actually use observational data was used. The preliminary work of Weinzapfel and Leslie (2003, 2004) using a similar configuration of ADAS to the one in this study on the case of a landfalling tropical cyclone showed only a limited impact of the cloud analysis beyond the first few hours of the forecast. In contrast, a case using a similar version of the complex cloud-analysis code used in ADAS on the 28 March 2000 Fort Worth, Texas, tornadic supercell event (Hu et al. 2006a,b) showed that individual supercells were not predicted at all without the help of a cloud analysis; very good matches of individual storm cells between the forecast and observation are obtained after cycled cloud analyses are performed, in that case, using data from a single WSR-88D. The positive impact lasted for about 2 h in their case.

In our case, the clear positive impact of cloud analysis lasts for more than 9 h although the MCS also develops in the forecasts without a cloud analysis. Thus the impact of a cloud analysis appears flow and scale dependent and depends on how strongly the predicted system is forced by well-analyzed scales of motion in the initial condition. The impact appears to be inversely proportional to the scale of the phenomena being predicted and/or the strength of the larger-scale forcing. It also appears to be dependent on whether or not a well-organized system is present at the initial time of the model forecast, as might be expected, and as seen from the results of the 1800 UTC forecasts. We suggest that the significant positive impact on our forecast is due primarily to the type of convective system in our study. A self-sustaining and self-propagating system such as the MCS in this study would be more likely to benefit from a more accurate analysis of the initial cloud structure than a tropical cyclone, whose precipitation fields are to a much larger degree driven by larger-scale dynamical processes. The prediction of this same MCS, however, would also be expected to be less affected by a cloud analysis than the forecast of weakly forced individual convective storms, as is the case in the study of Hu et al. (2006a,b). Still, the mesoscale forcing is not

completely absent from the analyses using conventional data alone; therefore the MCS still develops without a cloud analysis.

For the cases that did not include an initial cloud analysis, it is less clear why the use of additional extra surface data in the initial conditions does not appear to produce a significant positive impact on the forecast in terms of either position error or ETS, although an improvement in both, at least for the first half of the forecast in terms of the position error, is seen when additional standard data is used over that of the Eta analysis (i.e., 3km00ZSt versus 3km00ZEta). It appears that this issue is related to the spinup time of the MCS in the model, which is not properly analyzed in the non-cloud-analysis forecasts. To examine this issue in more detail, plots of surface potential temperature, surface convergence, and composite reflectivity for both the initial time, and after 1.5 h of forecast, are shown for 3km00ZEta and 3km00ZSt in Fig. 16. The corresponding fields for 3km00ZExt are very similar to those of 3km00ZSt and are thus not shown. In each case, there is no nonzero reflectivity at the initial time near the region of maximum surface convergence near the center of the surface low in the north-central Texas panhandle, and the convergence is slightly weaker in 3km00ZEta than in 3km00ZSt. Furthermore, the leading edge of the cold pool (represented by the 300-K potential temperature contour) extends to near the center of the surface low in 3km00ZSt (Fig. 16a) but is incorrectly analyzed too far to the northeast, mostly within Kansas, in 3km00ZEta (Fig. 16b). Given the location of the leading convective line across the northern Texas panhandle into extreme northern Oklahoma at this time (cf. Fig. 8a), the representation of the cold pool and corresponding strong northerly surface outflow winds in 3km00ZSt is regarded as being more accurate. After 1.5 h, the model has spun up reflectivity in both forecasts, but the convection is considerably more developed, and the surface convergence line just south of the surface low is significantly stronger in 3km00ZSt than in 3km00ZEta. In 3km00ZSt, the leading edge of the cold pool east of the surface low had reached western central Oklahoma by 0130 UTC but that in 3km00ZEta remained at the Oklahoma–Kansas border at this time. It appears that the strong convective cell that has developed in 3km00ZSt in the eastern Texas panhandle by this time was aided by the interaction of this leading edge of cold pool with the enhanced convergence line south of the surface low (Fig. 16d). In 3km00ZEta, some reflectivity has also begun to develop in this general region and has begun to form a weak cold pool over the Texas panhandle, as can be seen by the diverging surface flow in this region. How-

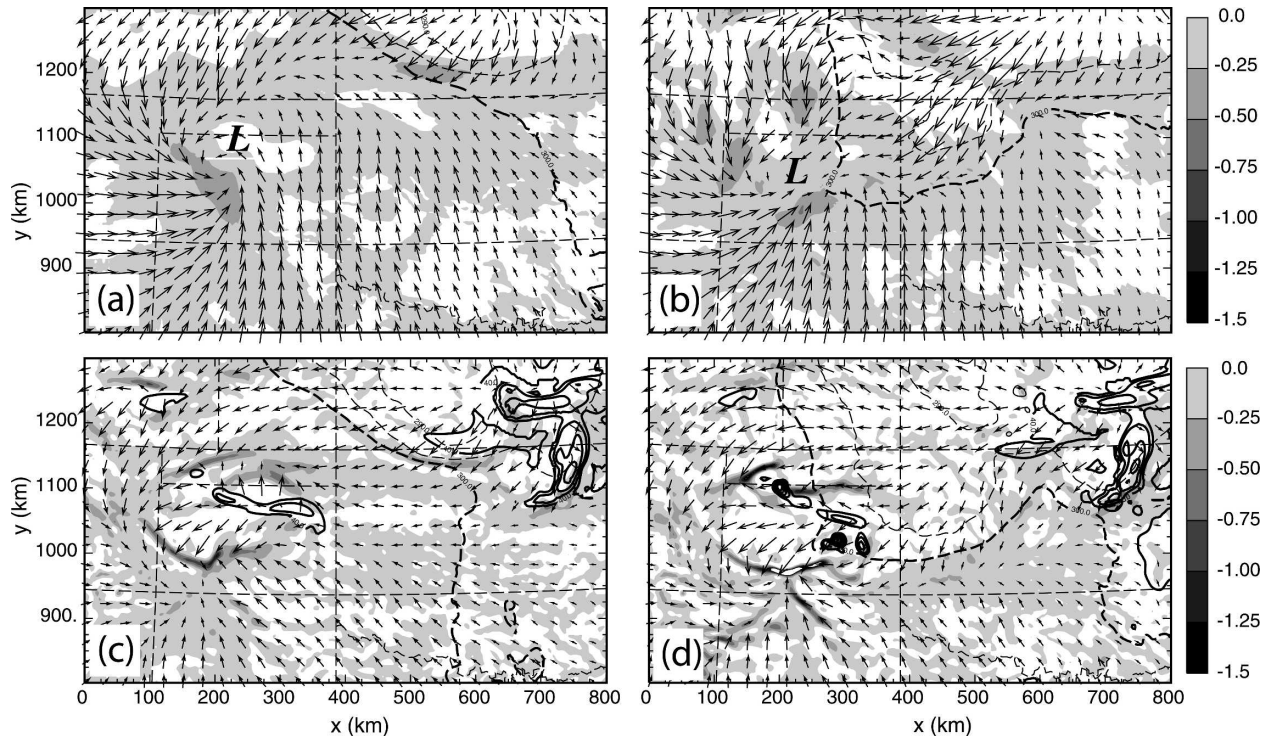


FIG. 16. Plots of surface convergence (shaded in units of 1000 s^{-1}) for (a) 3km00Zeta at the initial forecast time (0000 UTC 16 Jun 2002), (b) 3km00Zst at the initial forecast time, (c) 3km00Zeta at 1.5 h into the forecast (0130 UTC), and (d) 3km00Zst at 1.5 h into the forecast. Also shown are contours of potential temperature in 5-K increments from 300 K down (dashed contours), contours of composite reflectivity in 5 dBZ starting at 40 dBZ (solid contours), and wind vectors plotted every 30 km, with the length of one interval representing 10 m s^{-1} .

ever, the strong convective cell present in 3km00Zst is absent in 3km00Zeta at this time, though it does eventually develop by 2 h into the forecast (not shown). Apparently, the much improved analysis of the cold pool in the initial condition of 3km00Zst, using surface data, as well as the improved analysis of the circulation associated with surface low, led to earlier and more correct development of the convection in 3km00Zst (consistent with Fig. 10), and therefore an improved forecast of the evolution and propagation of the MCS. On the other hand, the addition of extra data in 3km00ZExt, over the standard data sources used by 3km00Zst, did not appear to significantly alter the surface convergence fields or the analysis of the cold pool, at least in this case near the point of convective initiation (not shown), which helps to explain the general lack of further improvement in the ETS and position forecasts of the MCS.

7. Summary and future work

In this study, we report on a set of high-resolution forecasts of a severe MCS case that occurred during the

field experiment period of IHOP_2002 (Weckwerth et al. 2004). The forecasts were designed to test the impact of the use of different data networks in the initial conditions of the model forecasts, the use of a complex cloud-analysis scheme, and the use of high-frequency intermittent assimilation cycles. All experiments were able to produce a strong MCS in the model, and the general structure and behavior were similar to those of the observed MCS, particularly in terms of the propagation direction and speed. This suggests that the synoptic and mesoscale environment for this case was strongly supportive of the development of a long-lived bow-echo-type MCS, largely independent of the fine-scale details of the initial conditions, or whether or not a cloud analysis is performed. Certain larger-scale forcing mechanisms, such as the forcing from the upper-level jet streak and the surface cold front associated with the surface low over the Texas panhandle region were likely important to the initial development of the MCS in this case. More study on the particular initiation mechanisms for this system, to better determine to what extent the synoptic-scale flow was important, is needed. In contrast, in the previously studied Fort Worth tor-

nadic thunderstorm case (Hu et al. 2006a,b), the forecast of weakly forced individual convective elements was strongly dependent on the presence or absence of a cloud-analysis procedure, using radar data.

Notwithstanding the above considerations, the forecasts that incorporated a cloud analysis using data from multiple-Doppler radars in the initial conditions were superior to those that did not for the case of 0000 UTC 16 June 2002 forecasts, in which a well-defined bow echo was present at the initial time. This is confirmed by the results of an analysis of the position errors of the MCS at various forecast times, and by the ETSs of composite reflectivity. The superior forecast in the case of the cloud analysis runs was primarily due to the removal of the otherwise needed spinup time of the convective system in the model, whereas the convection in the forecasts that contained no cloud analysis all took between 2 to 3 h to spin up. Also, the use of additional observational data in the initial analysis over that of the Eta analysis, but without cloud analysis, was shown to reduce the spinup time of the system by about 1 h. It was shown that in such a case the stronger surface convergence near the leading edge of the cold pool, as well as the analyzed cold pool itself, in the initial conditions appears to be responsible for this reduced spinup time. However, this improvement in the spinup time from the use of additional surface data did not lead to a significantly improved ETS for composite reflectivity.

On the other hand, results from the set of forecasts starting from 1800 UTC show that the cloud analysis has much less of an impact at this time, and in fact the improvement in the ETSs is virtually nonexistent. This is also consistent with earlier work in which a start time of 1200 UTC was used (Dawson and Xue 2004). We suggest that this is due mostly to the lack of a well-defined MCS at the initial time. Although several areas of disorganized convection were present at this time, the individual convective lines that later developed and merged to form the bow echo were either not present or just beginning to develop by 1800 UTC. This also seems to be the reason that the forecasts incorporating a 3-h assimilation window with 30-min intervals from 1500 to 1800 UTC also failed to show an improved forecast over that of the cold start runs starting from 1800 UTC. The limitations of the current analysis procedure and the predictability of convective elements beyond their life cycles may explain some of these behaviors. More advanced data assimilation techniques such as the 4DVAR and ensemble Kalman filter may demonstrate a more significant impact of the extra and radar data, and the benefit of assimilation cycles. We are actively working on the latter technique.

Acknowledgments. This work was supported by NSF Grant ATM-0129892 and by the National Defense Science and Engineering Graduate Fellowship, and NSF Graduate Research Fellowship. Ming Xue was also supported by NSF Grants EEC-0313747, ATM-0331594, and ATM-0530814 and by a DOT-FAA grant via DOC-NOAA NA17RJ1227. The authors thank the OU Supercomputing Center for Education and Research (OSCER) for the use of its massively parallel Linux cluster. Some of the simulations were also performed on the National Science Foundation Terascale Computing System at the Pittsburgh Supercomputing Center.

REFERENCES

- Baldwin, M. E., S. Lakshminarayanan, and J. S. Kain, 2001: Verification of mesoscale features in NWP models. Preprints, *Ninth Conf. on Mesoscale Processes*, Fort Lauderdale, FL, Amer. Meteor. Soc., 255–257.
- , —, and —, 2002: Development of an “events-oriented” approach to forecast verification. Preprints, *15th Conf. on Numerical Weather Prediction*, San Antonio, TX, Amer. Meteor. Soc., CD-ROM, 7B.3.
- Bratseth, A. M., 1986: Statistical interpolation by means of successive corrections. *Tellus*, **38A**, 439–447.
- Brewster, K., 1996: Application of a Bratseth analysis scheme including Doppler radar data. Preprints, *15th Conf. on Weather Analysis and Forecasting*, Norfolk, VA, Amer. Meteor. Soc., 92–95.
- , 2002: Recent advances in the diabatic initialization of a non-hydrostatic numerical model. Preprints, *15th Conf. on Numerical Weather Prediction and 21st Conf. on Severe Local Storms*, San Antonio, TX, Amer. Meteor. Soc., CD-ROM, J6.3.
- Case, J. L., J. Manobianco, T. D. Oram, T. Garner, P. F. Blottman, and S. M. Spratt, 2002: Local data integration over east-central Florida using the ARPS Data Analysis System. *Wea. Forecasting*, **17**, 3–26.
- Courtier, P., and Coauthors, 1998: The ECMWF implementation of three-dimensional variational assimilation (3D-Var). I: Formulation. *Quart. J. Roy. Meteor. Soc.*, **124**, 1783–1808.
- Dawson, D. T., II, and M. Xue, 2004: Impact of mesoscale data, cloud analysis on the explicit prediction of a MCS during IHOP 2002. *Extended Abstracts, 20th Conf. on Weather Analysis and Forecasting/16th Conf. on Numerical Weather Prediction*, Seattle, WA, Amer. Meteor. Soc., CD-ROM, P1.36.
- Dowell, D., F. Zhang, L. J. Wicker, C. Snyder, and N. A. Crook, 2004: Wind and temperature retrievals in the 17 May 1981 Arcadia, Oklahoma, supercell: Ensemble Kalman filter experiments. *Mon. Wea. Rev.*, **132**, 1982–2005.
- Ebert, E., and J. McBride, 2000: Verification of precipitation in weather systems: Determination of systematic errors. *J. Hydrol.*, **239**, 179–202.
- Gao, J.-D., M. Xue, K. Brewster, and K. K. Droegemeier, 2004: A three-dimensional variational data analysis method with recursive filter for Doppler radars. *J. Atmos. Oceanic Technol.*, **21**, 457–469.
- Hu, M., M. Xue, and K. Brewster, 2006a: 3DVAR and cloud analysis with WSR-88D level-II data for the prediction of

- Fort Worth, Texas, tornadic thunderstorms. Part I: Cloud analysis and its impact. *Mon. Wea. Rev.*, **134**, 675–698.
- , —, J. Gao, and K. Brewster, 2006b: 3DVAR and cloud analysis with WSR-88D Level-II data for the prediction of Fort Worth, Texas, Tornadic Thunderstorms. Part II: Impact of radial velocity analysis via 3DVAR. *Mon. Wea. Rev.*, **134**, 699–721.
- Kain, J. S., M. E. Baldwin, and S. J. Weiss, 2003: Parameterized updraft mass flux as a predictor of convective intensity. *Wea. Forecasting*, **18**, 106–116.
- Lazarus, S., C. M. Ciliberti, J. D. Horel, and K. Brewster, 2002: Near-real-time applications of a mesoscale analysis system to complex terrain. *Wea. Forecasting*, **17**, 971–1000.
- Lorenc, A. C., 1981: A global three-dimensional multivariate statistical interpolation scheme. *Mon. Wea. Rev.*, **109**, 701–721.
- Nachamkin, J. E., 2004: Mesoscale verification using meteorological composites. *Mon. Wea. Rev.*, **132**, 941–955.
- Parrish, D. F., and J. C. Derber, 1992: The National Meteorological Center's spectral statistical-interpolation analysis system. *Mon. Wea. Rev.*, **120**, 1747–1763.
- Rabier, F., H. Jarvinen, E. Klinker, J.-F. Mahfouf, and A. Simmons, 2000: The ECMWF operational implementation of four-dimensional variational assimilation. I: Experimental results with simplified physics. *Quart. J. Roy. Meteor. Soc.*, **126**, 1143–1170.
- Schaefer, J. T., 1990: The critical success index as an indicator of warning skill. *Wea. Forecasting*, **5**, 570–575.
- Smith, P. L., Jr., C. G. Myers, and H. D. Orville, 1975: Radar reflectivity factor calculations in numerical cloud models using bulk parameterization of precipitation processes. *J. Appl. Meteor.*, **14**, 1156–1165.
- Snyder, C., and F. Zhang, 2003: Assimilation of simulated Doppler radar observations with an ensemble Kalman filter. *Mon. Wea. Rev.*, **131**, 1663–1677.
- Souto, M. J., C. F. Balseiro, V. Pérez-Muñuzuri, M. Xue, and K. Brewster, 2003: Importance of cloud analysis and impact for daily forecast in terms of climatology of Galician region, Spain. *J. Appl. Meteor.*, **42**, 129–140.
- Sun, J., and N. A. Crook, 2001: Real-time low-level wind and temperature analysis using single WSR-88D data. *Wea. Forecasting*, **16**, 117–132.
- Tong, M., and M. Xue, 2005: Ensemble Kalman filter assimilation of Doppler radar data with a compressible nonhydrostatic model: OSS experiments. *Mon. Wea. Rev.*, **133**, 1789–1807.
- Weckwerth, T. M., and Coauthors, 2004: An overview of the International H2O Project (IHOP_2002) and some preliminary highlights. *Bull. Amer. Meteor. Soc.*, **85**, 253–277.
- Weinzapfel, B. A., and L. Leslie, 2003: A very high resolution simulation of Tropical Storm Allison, June 2001. Preprints, *12th Conf. on Interactions of the Sea and Atmosphere*, Long Beach, CA, Amer. Meteor. Soc., CD-ROM, P5.6.
- , and —, 2004: A high-resolution, local-domain numerical modeling study of a flooding rainfall event associated with Tropical Storm Allison in June 2001 over Houston, Texas. Preprints, *Symp. on Planning, Nowcasting, and Forecasting in the Urban Zone*, Seattle, WA, Amer. Meteor. Soc., CD-ROM, 1.5.
- Xue, M., K. K. Droegemeier, and V. Wong, 2000: The Advanced Regional Prediction System (ARPS)—A multiscale nonhydrostatic atmospheric simulation and prediction tool. Part I: Model dynamics and verification. *Meteor. Atmos. Phys.*, **75**, 161–193.
- , and Coauthors, 2001: The Advanced Regional Prediction System (ARPS)—A multi-scale nonhydrostatic atmospheric simulation and prediction tool. Part II: Model physics and applications. *Meteor. Atmos. Phys.*, **76**, 143–166.
- , D.-H. Wang, J.-D. Gao, K. Brewster, and K. K. Droegemeier, 2003: The Advanced Regional Prediction System (ARPS), storm-scale numerical weather prediction and data assimilation. *Meteor. Atmos. Phys.*, **82**, 139–170.
- Zhang, J., 1999: Moisture and diabatic initialization based on radar and satellite observation. Ph.D. thesis, University of Oklahoma, 194 pp.
- , and F. Carr, 1998: Moisture and latent heating rate retrieval from radar data. Preprints, *12th Conf. on Numerical Weather Prediction*, Phoenix, AZ, Amer. Meteor. Soc., 205–208.
- , —, and K. Brewster, 1998: ADAS cloud analysis. Preprints, *12th Conf. on Numerical Weather Prediction*, Phoenix, AZ, Amer. Meteor. Soc., 185–188.